Fluorescence Spectroscopy In Vivo

Nirmala Ramanujam

Fluorescence Spectroscopy In Vivo

Nirmala Ramanujam
University of Wisconsin, Madison, USA

Diagnostic techniques based on optical spectroscopy have the potential to link the biochemical and morphological properties of tissues to individual patient care. In particular, these techniques are fast, noninvasive and quantitative. Furthermore, they can be used to elucidate key tissue features, such as the cellular metabolic rate, vascularity, intravascular oxygenation and alterations in tissue morphology. These tissue features can be interpreted to shed light on a variety of clinical problems, such as precancerous and cancerous growth and atherosclerosis. The goal of this report is to review the development and application of optical spectroscopy in the ultraviolet (UV) and visible (VIS) spectral regions, as a diagnostic tool in clinical applications. A particular emphasis is placed on steady-state, UV/VIS fluorescence spectroscopy for the detection of precancers and cancers, in vivo.

1 FLUORESCENCE SPECTROSCOPY

1.1 Introduction

Diagnostic techniques based on optical spectroscopy have the potential to link the biochemical and morphological properties of tissues to individual patient care. In particular, these techniques are fast, noninvasive and quantitative. Furthermore, they can be used to elucidate key tissue features, such as the cellular metabolic rate, vascularity, intravascular oxygenation and alterations in tissue morphology. These tissue features can be interpreted to shed light on a variety of clinical problems, such as precancerous and cancerous growth and atherosclerosis.[1] If applied successfully, optical spectroscopy has the potential to represent an important step forward toward advances in diagnostic and therapeutic medical applications.

Spectroscopy is the study of the interaction of electromagnetic radiation with matter. There are three aspects to a spectroscopic measurement: irradiation of a sample with electromagnetic radiation; measurement of the absorption, spontaneous emission (fluorescence, phosphorescence) and/or scattering (Rayleigh elastic

scattering, Raman inelastic scattering) from the sample; and analysis and interpretation of these measurements. Detailed study of absorption, spontaneous emission and scattering provides information that can be classified broadly as analytical, structural, dynamic, and energetic.[2]

Optical spectroscopy deals with interactions of electromagnetic radiation with matter that occur at the UV, VIS, near-infrared (NIR) and infrared (IR) wavelengths. In the UV/VIS spectral regions (<700 nm), light can penetrate only superficial tissue volumes (a few hundred microns to a millimeter in depth) due to the fact that this biological medium is highly absorbing.[3] However, in the NIR spectral region (700–900 nm) tissue is generally less absorbing and, furthermore, the number of elastic scattering events of light in tissue is approximately two orders of magnitude greater than the number of absorption events.[4] This enables the light to propagate through tissue volumes that are up to several centimeters in depth.

In the UV/VIS spectral regions, absorption and fluorescence spectroscopy have been explored extensively as diagnostic tools for precancer and cancer detection in the surface epithelia of various organ sites (colon, cervix, bronchus, lung, bladder, brain, esophagus, head and neck, skin, bile duct, breast and stomach tissues)[5–12] and for the characterization of atherosclerosis in the surface of artery vessel walls.[5,6,11] Recently, fluorescence spectroscopy was also used to detect Alzheimer's disease of the brain in vitro.[13] Elastic scattering spectroscopy in this spectral region also has been evaluated for the detection of precancers and cancers in the surface epithelia of several organ sites, but to a much lesser extent.[14]

NIR absorption,[4] fluorescence and phosphorescence[15] spectroscopies have been used to interrogate larger tissue volumes. In particular, NIR absorption has been used to detect brain bleeds,[16] brain oxygenation,[17] functional activity of the brain,[18,19] bioenergetics of skeletal muscle (e.g. in the case of genetic disease of mitochondrial function)[20] and breast tumors.[21] NIR correlation spectroscopy, which monitors fluctuations in the elastic scatter intensity, is emerging as a potential diagnostic tool to detect blood flow deep within thick tissue.[22]

To date, most clinical applications have concentrated on absorption, fluorescence and elastic scattering spectroscopies, because these measurements can be obtained with a good signal-to-noise ratio in reasonably short integration times. However, with advances in illumination and detection technologies, NIR Raman scattering, which is a relatively weak phenomenon, is emerging as a potential diagnostic tool for precancer and cancer detection in the surface epithelia of various organ sites,[23] for the characterization of atherosclerosis on the surface of artery vessel walls[24] and for glucose monitoring.[25]

The goal of this article is to review the development and application of UV/VIS optical spectroscopy as a diagnostic tool in clinical applications. Particular emphasis is placed on steady-state UV/VIS fluorescence spectroscopy for the detection of precancers and cancers in vivo. In this section the principles and definitions that are related to the phenomenon of fluorescence are summarized. In the next section the endogenous fluorescence properties of molecules present in cells and tissues and the fluorescence properties of exogenous molecules, which can be used as contrast agents, are presented. This is followed in section 3 by a discussion of the effect of absorption and scattering on fluorescence spectroscopy of turbid media such as tissue, and methods for deconvolving this effect. Next, the instrumentation requirements for fluorescence spectroscopy of tissues are reviewed in section 4. In the last several sections, a summary of the clinical applications of fluorescence spectroscopy, particularly precancer and cancer detection (section 5), a review of representative instruments (section 6) and methods of analysis used (section 7) are presented. With respect to methods of analysis, statistical models, which are used solely for the purpose of discriminating diseased from nondiseased tissues based on the spectral information, as well as physical models, which have the potential to elucidate the biochemical/morphological basis for the spectral differences observed, are presented. In the final part of section 7, the effect of the illumination and collection geometry on fluorescence spectroscopy of tissues is discussed and approaches to resolve it are presented. This article concludes with a brief discussion of future perspectives in section 8.

1.2 Principles and Definitions

1.2.1 Probing Energy Levels with Electromagnetic Radiation

Optical spectroscopy probes the energy levels of a molecule.[2] The energy level of a molecule is defined as its characteristic state, which is related to the molecular structure of the molecule and to the energetics and dynamics of any chemical processes that the molecule may undergo. The ground state of a molecule is defined as the state of lowest energy. States of higher energy are called excited states. A molecule possesses several distinct reservoirs of energy levels, including electronic, vibrational, rotational, translational and those associated with nuclear and electron spin.[2] In the optical regime, the energy levels of interest are those that are associated with vibrational and electronic transitions. The separation between vibrational energy levels is determined by the mass of the atoms and the flexibility of the chemical bonds joining them. The separation between electronic

energy levels, which is greater, occurs when electrons are displaced from one region of a molecule to another.

At any finite temperature, the molecules will be distributed among the energy levels available to them because of thermal agitation.[2] The exact distribution will depend on the temperature (T) and on the separation between the energy levels (ΔE) in the energy ladder. At a given temperature, the number of molecules in an upper level (n_{upper}) relative to that in a lower level (n_{lower}) is given by the Boltzmann distribution, as shown in Equation (1):

$$\frac{n_{upper}}{n_{lower}} = \exp\left(\frac{-\Delta E}{kT}\right) \tag{1}$$

where k is the Boltzmann constant ($1.38 \times 10^{-23}\,\text{J K}^{-1}$). When electromagnetic radiation is applied to a molecule, it is just as likely to cause transitions from a higher to a lower energy level as it is to cause transitions from a lower to a higher energy level. Consequently, net absorption or transition to a higher energy level can occur only if the difference between the populations of the energy levels concerned is significant, with the lower one being significantly higher. Calculation of the population of energy levels at room temperature[2] has shown that for vibrational energy level spacings the ratio n_{upper}/n_{lower} is $\sim 10^{-3}$ and for electronic energy level spacings it is 10^{-21}.

1.2.2 The Fluorescence Phenomenon

Figure 1 displays an energy level diagram with ground (S_0) and excited (S_1) electronic states as well as vibrational energy levels within each electronic state of a molecule.[26] When a molecule is illuminated at an excitation wavelength that lies within the absorption spectrum of that molecule, it will absorb the energy and be activated from its ground state (S_0) to an excited singlet state (S_1), with the electron in the same spin as its ground state. The molecule can then relax back from the excited state to the ground state by generating energy either nonradiatively or radiatively, depending on the local environment. In a nonradiative transition, relaxation occurs
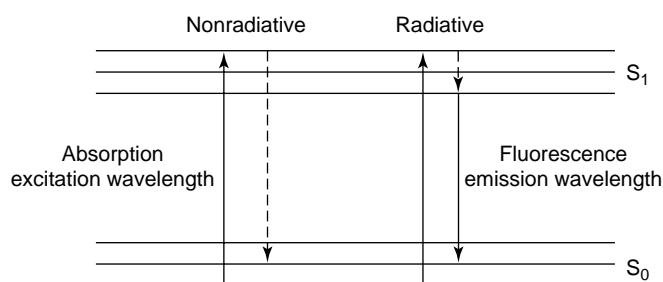
by thermal generation (dashed arrows). In a radiative transition, relaxation occurs via fluorescence at specific emission wavelengths (solid arrow). Fluorescence generation occurs in three steps: thermal equilibrium is achieved rapidly as the electron makes a nonradiative transition to the lowest vibrational level of the first excited state; the electron then makes a radiative transition to a vibrational level of the ground state; and finally the electron makes a nonradiative transition to the lowest vibrational level of the ground state. When there is inter-system crossing, in which the spin of the electron is flipped in the excited state, the time for radiative transition from the excited state to ground state is longer because the transition must occur with a spin change. This excited state is termed the triplet state (not shown). Radiative transition from the excited triplet state is termed phosphorescence. Tissue absorption, fluorescence and phosphorescence monitor changes in electronic energy levels, to provide biochemical information from biological molecules.

The phenomenon of fluorescence displays several general characteristics for a particular biological molecule.[26] First, due to the losses in energy between absorption and emission that occur as a result of nonradiative transitions, fluorescence occurs at emission wavelengths that are always red-shifted relative to the excitation wavelength. Second, the emission wavelengths are independent of the excitation wavelength. Third, the fluorescence spectrum of a biological molecule is generally a mirror image of its absorption spectrum.

The fluorescence of a biological molecule is characterized by its quantum yield and its lifetime.[26] The quantum yield is simply the ratio of the number of photons emitted to the number absorbed. The lifetime is defined as the average time the biological molecule spends in the excited state prior to return to the ground state. The fluorescence quantum yield and lifetime are modified by a number of factors that can increase or decrease the energy losses. For example, a molecule may be nonfluorescent as a result of a large rate of nonradiative decay (thermal generation) or a slow rate of radiative decay (fluorescence generation).

Fluorescence spectroscopy is the measurement and analysis of various features that are related to the fluorescence quantum yield and/or lifetime of a biological molecule. The fluorescence intensity of a biological molecule is a function of its concentration, its extinction coefficient (absorbing power) at the excitation wavelength, and its quantum yield at the emission wavelength.[2] A fluorescence emission spectrum represents the fluorescence intensity measured over a range of emission wavelengths at a fixed excitation wavelength. On the other hand, a fluorescence excitation spectrum is a plot of the fluorescence intensity at a particular emission wavelength for a range of excitation wavelengths.
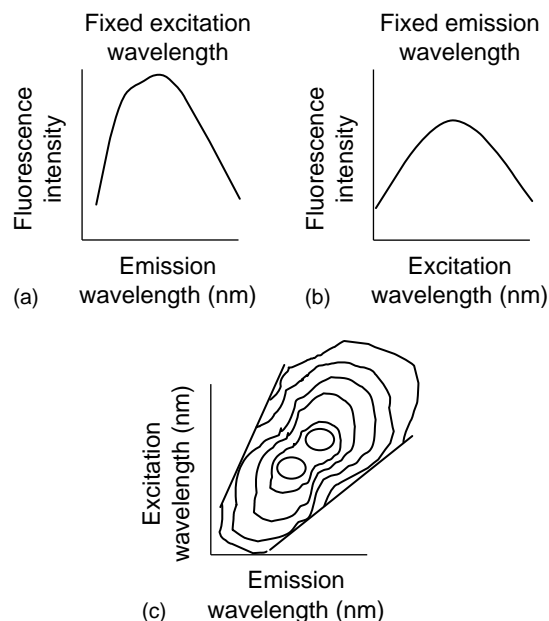

Figure 1 Energy level diagram illustrating the phenomena of absorption and fluorescence of a molecule.

Figure 2 Illustration of: (a) a fluorescence emission spectrum; (b) a fluorescence excitation spectrum; (c) an EEM of a molecule.

A fluorescence excitation–emission matrix (EEM) is a two-dimensional contour plot that displays the fluorescence intensities as a function of a range of excitation and emission wavelengths. Each contour represents points of equal fluorescence intensity. Figure 2 illustrates a fluorescence emission spectrum (Figure 2a), a fluorescence excitation spectrum (Figure 2b) and a fluorescence EEM (Figure 2c).

2 FLUOROPHORES

2.1 Endogenous Fluorophores

Table 1 lists the biological molecules that exhibit endogenous fluorescence, along with their excitation and emission maxima.[11,27] These endogenous fluorophores include amino acids, structural proteins, enzymes and co-enzymes, vitamins, lipids and porphyrins. Their excitation maxima lie in the range 250–450 nm (spanning the UV/VIS spectral range), whereas their emission maxima lie in the range 280–700 nm (spanning the UV/VIS/NIR spectral range). Details of the molar extinction coefficients, fluorescence quantum yields and lifetimes are provided elsewhere.[11] The endogenous fluorophores that are speculated to play a role in transformations that occur with carcinogenesis are the amino acids tryptophan and tyrosine,[28,29] the structural proteins collagen and elastin,[30–36] the coenzymes NADH[28,37] and FAD,[37,38] and porphyrins.[39]

Table 1 Excitation and emission maxima of biological molecules that exhibit endogenous fluorescence

Endogenous fluorophores	Excitation maxima (nm)	Emission maxima (nm)
Amino acids		
Tryptophan	280	350
Tyrosine	275	300
Phenylalanine	260	280
Structural proteins		
Collagen	325	400, 405
Elastin	290, 325	340, 400
Enzymes and coenzymes		
FAD, flavins	450	535
NADH	290, 351	440, 460
NADPH	336	464
Vitamins		
Vitamin A	327	510
Vitamin K	335	480
Vitamin D	390	480
Vitamin B$_6$ compounds		
Pyridoxine	332, 340	400
Pyridoxamine	335	400
Pyridoxal	330	385
Pyridoxic acid	315	425
Pyridoxal 5′-phosphate	330	400
Vitamin B$_{12}$	275	305
Lipids		
Phospholipids	436	540, 560
Lipofuscin	340–395	540, 430–460
Ceroid	340–395	430–460, 540
Porphyrins	400–450	630, 690

FAD, flavin adenine dinucleotide; NADH, reduced nicotinamide adenine dinucleotide; AND(P)H, reduced nicotinamide adenine dinucleotide phosphate.

2.1.1 Amino Acids: Tryptophan and Tyrosine

Amino acids are the basic structural units of a protein[40] and proteins play crucial roles in virtually all of the biological processes.[40] Three amino acids with aromatic side chains are fluorescent. At excitation wavelengths above 295 nm only tryptophan is fluorescent.[26] From 280 to 295 nm, both tyrosine and tryptophan are fluorescent; however, energy transfer from tryptophan to tyrosine is common.[26] Below 280 nm, all three amino acids can be excited, albeit the quantum yield of phenylalanine is relatively low compared with that of tryptophan and tyrosine.[26]

2.1.2 Structural Proteins: Collagen and Elastin

Collagen, a family of fibrous proteins, is distinctive in forming insoluble fibers that have a high tensile strength.[40] It is the major extracellular matrix component that is present to some extent in nearly all organs

and serves to hold cells together in discrete units. Elastin is the major component of elastic fibers and is found in most connective tissues in conjunction with collagen and polysaccharides.[40]

Fluorescence has been noted from collagen[41] and elastin.[42] Collagen fluorescence in load-bearing tissues is associated with cross-links, hydroxylysyl pyridoline and lysyl pyridinoline.[43] Collagen fluorescence has an excitation maximum at 325 nm and an emission maximum at 400 nm, as displayed in Figure 3.[41] The fluorescent material in elastin is a tricarboxylic triamino pyridinium derivative, which is very similar in spectral properties to the fluorophore in collagen.[44] The excitation and emission maxima of the fluorescence of this elastin cross-link occur at 320 and 405 nm, respectively, as shown in Figure 4.[42]

2.1.3 Metabolic Coenzymes: Pyridine Nucleotides and Flavoproteins

Living organisms require a continual input of free energy through cellular metabolism for the performance of mechanical work in muscle contraction and other cellular movements, the active transport of molecules and ions, and the synthesis of macromolecules and other biomolecules from simple precursors.[40] In most processes, the carrier of free energy is adenosine triphosphate (ATP), which is derived from the oxidation of fuel molecules such as carbohydrates and fatty acids. In aerobic organisms, the ultimate oxidizing agent or electron acceptor is molecular oxygen. However, electrons are not transferred directly from fuel molecules and their breakdown products to molecular oxygen. Instead, these substrates transfer electrons to special
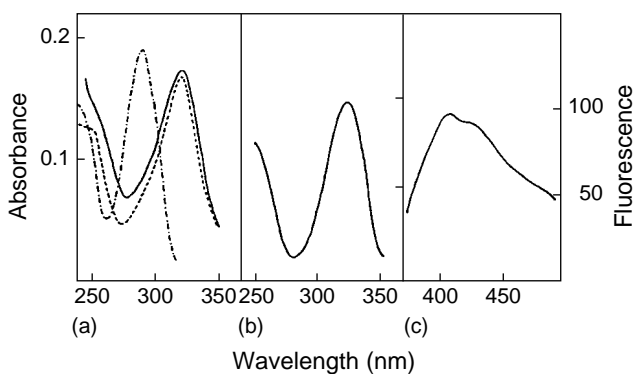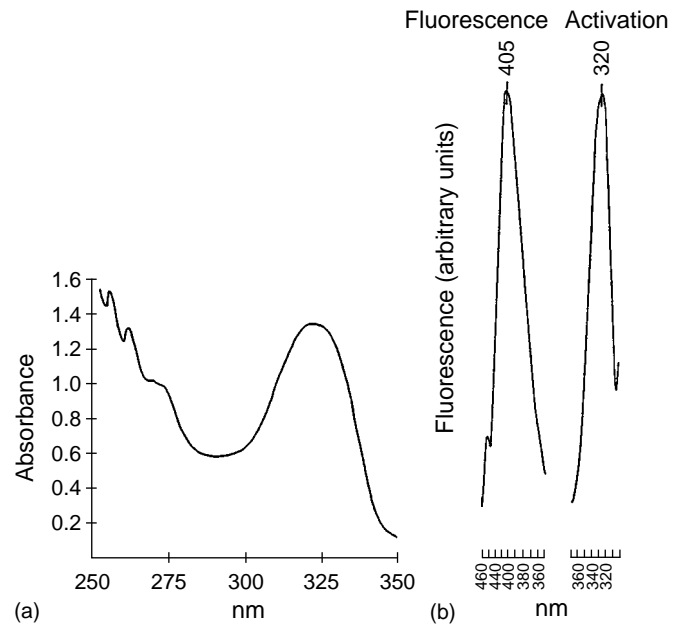

Figure 4 Elastin fluorescence: (a) UV absorption spectrum in 0.1 M potassium phosphate buffer; (b) fluorescence emission and excitation (activation) spectrum in 0.1 M HCl. (Reprinted from Deyl et al.,[42] with permission from Elsevier Science.)

carriers called pyridine nucleotide (PN) and flavoprotein (Fp). The oxidized form of PN – nicotinamide adenine dinucleotide (NAD^+) – and the oxidized form of Fp/FAD – are the major electron acceptors in the oxidation of fuel molecules. After accepting the electrons, these carriers become reduced. The now reduced electron carriers – NADH and reduced flavin adenine dinucleotide ($FADH_2$) – then transfer their electrons to molecular oxygen by means of the electron transport chain in the inner membrane of the mitochondria within the cell. As a result, molecular oxygen oxidizes them to NAD^+ and FAD. The ultimate flow of these electrons to molecular oxygen drives the synthesis of ATP.

The fluorescent forms of these electron carriers are the reduced form of PN and the oxidized form of Fp, which emit fluorescence when excited with UV and blue light respectively. Figure 5 displays the fluorescence excitation and emission spectra of Fp and PN from isolated pigeon heart mitochondria measured at $-196\,^\circ$C.[45] Figure 5(a) and (b) displays the oxidized (Ox) and reduced (Red) Fp excitation and emission spectra, respectively, and Figure 5(c) and (d) shows the oxidized (Ox) and reduced (Red) PN excitation and emission spectra, respectively. Clearly, the excitation and emission of Fp is maximal when it is oxidized and minimal when it is reduced. The converse is true for PN. The ratio of the concentration of oxidized and reduced electron carriers (or, synonymously, the ratio of the fluorescence of Fp and PN) gives a measure of the cellular metabolic rate.[45] In particular, a reduced

Figure 3 Collagen fluorescence: (a) UV absorption spectra in 0.1 N HCl (------), in 0.1 M potassium phosphate buffer, pH 7.4 (- - -), and in 0.1 N NaOH (——); (b) fluorescence excitation spectrum in 0.02 M potassium phosphate buffer, pH 7.4, with emission fixed at 400 nm; (c) fluorescence emission spectrum in 0.02 M potassium phosphate buffer, pH 7.4, with excitation fixed at 325 nm. (Reproduced by permission of Academic Press, Orlando, Florida, from Fujimoto.[41])
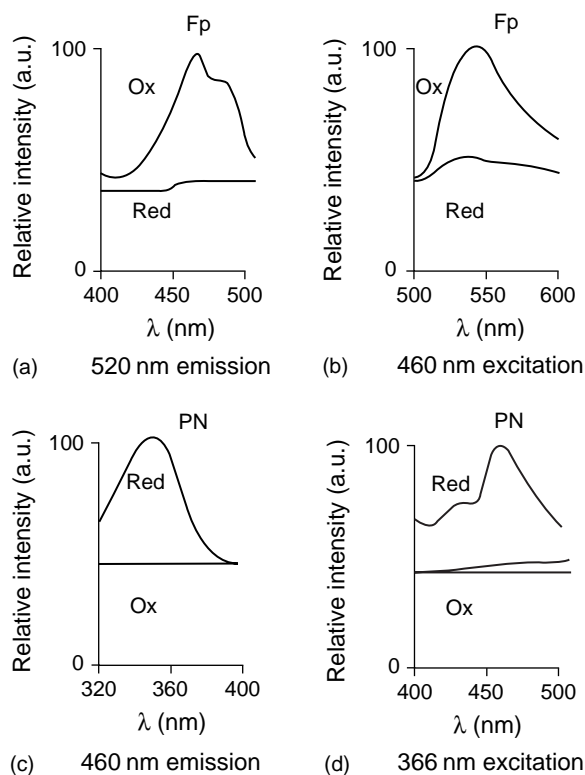
Figure 5 (a, b) The oxidized (Ox) and reduced (Red) Fp excitation and emission spectra, respectively. (c, d) The oxidized (Ox) and reduced (red) PN excitation and emission spectra, respectively. The measurements were made from pigeon heart mitochondria at −196 °C. (Reproduced by permission from Chance et al.[45])

ratio is indicative of a high phosphate potential (state 4), whereas an oxidized ratio indicates a low phosphate potential (states 2 and 3).

2.1.4 Porphyrins

Porphyrin is a precursor in heme biosynthesis.[40] It leads to the synthesis of protoporphyrin IX (PpIX), which acquires an atom to form heme. δ-Aminolevulinate synthase, the enzyme catalyzing the committed step in this pathway, is feedback inhibited by heme. Porphyrins produce a red fluorescence, with peaks at 630 and 690 nm, when excited in the blue spectral region between 400 and 450 nm.[46]

2.1.5 Fluorescence Microscopy and Spectroscopy of Microstructures in Cultured Cells and Tissue Sections

Fluorescence microscopy and spectroscopy of fluorescent micro-structures in cultured cells and optically thin, unstained, frozen tissue sections have indicated that differences in the fluorescence emission spectra of normal,

precancerous and cancerous tissues may be attributed to differences associated with several endogenous fluorophores within the various sublayers of these tissues. Pradhan et al.[28] suggested that there is an increase in NADH and tryptophan, whereas Anidjar et al.[38] reported that there is probably a decrease in FAD as cells progress from a normal to cancerous state. Romer et al.[30] and Fairman et al.[32] observed a decreased fluorescence intensity from the collagens in precancerous colon tissue sections relative to that in normal colon tissue sections. Bottiroli et al.[34] observed a red fluorescence in some parts of a tissue section that was from a cancerous colon. The red fluorescence that was observed by Bottiroli et al.[34] has been observed previously by several groups.[37,47–51]

2.2 Exogenous Fluorophores

Most exogenous fluorophores currently being evaluated as contrast agents for precancer and cancer detection include photosensitizers, developed originally for photodynamic therapy (PDT).[12] These include hematoporphyrin derivative (HpD), pheophorbide-a, meso-tetra-(hydroxyphenyl)-chlorin (MTHPC), benzo-porphyrin derivative (BPD), tin etiopurpurin (SnET2), hypercin and pthalocyanine.[12] These compounds have strong absorption characteristics in the blue spectral region or up to the highest Q-band at 635 nm, resulting in fluorescence between 625 and 675 nm.[12] These agents are generally administered systemically and the difference in accumulation of these exogenous fluorophores in tumor tissue relative to their normal counterpart appears to correlate with the differences in the vascularity of the two tissue types.[12] Lutetium texaphyrin is another photosensitizing agent that has absorption and fluorescence characteristics in the NIR spectral region.[12] This agent seems to be selectively phototoxic to tumors via apoptosis rather than necrosis (which results from vascular stasis), suggesting that this agent localizes in the cell.[12]

During the past few years an alternative concept has been introduced, which is based on the initial observations of Ghadially et al.,[51] who suggested using the photosensitizing precursor δ-aminolevulinic acid (5-ALA) to induce PpIX fluorescence in tumors. PpIX is characterized by an absorption maximum at 405 nm and fluorescence maxima at 630 and 700 nm.[52] The compound 5-ALA is a natural precursor of PpIX in the biosynthetic pathway for heme.[52] Normally, the synthesis of heme regulates the synthesis of PpIX through feedback control. However, the administration of 5-ALA bypasses this feedback and induces the accumulation of PpIX in tumor tissue. It has been suggested that deficiency in ferrochelatase (the enzyme required for conversion of PpIX to heme) in tumors results in accumulation of PpIX

in these tissues relative to normal tissue.[12] There are several advantages associated with using 5-ALA as a contrast agent. Both 5-ALA and PpIX are substances naturally present in the body, making the toxicity issue less critical. Furthermore, the drug can be administered conveniently both orally and topically.[12]

The use of photosensitizers as purely contrast agents has raised potential safety and toxicity concerns. Hence, recent work has examined nonphotosensitizing agents with similar absorption and fluorescence characteristics to photosensitizers for their potential to serve as contrast agents. Several exogenous fluorophores, including Nile blue and its derivatives and the caretenoporphyrins, have been shown to fulfil this criterion.[12] Nonphototoxic or weakly phototoxic exogenous fluorophores that are in routine clinical use currently are fluorescin (fluorescin angiography) and indocyanine green (cardiac output measurements and liver assessment), which have absorption and fluorescence characteristics in the VIS and NIR regions, respectively.[11] In clinical use, these drugs are injected into the vasculature, through which they are ultimately cleared.

3 FLUORESCENCE SPECTROSCOPY OF TURBID MEDIA

3.1 Fluorescence Spectroscopy of an Optically Dilute, Homogeneous Medium

Using the Beer–Lambert law,[2] one can express the fluorescence intensity of an optically dilute, homogeneous medium (sum of the optical densities at the excitation and emission wavelengths. Everywhere is less than unity)[26] as a linear function of the concentration of the fluorophores in that medium. Specifically, the fluorescence intensity, $F(\lambda_x, \lambda_m)$, at particular excitation (λ_x) and emission (λ_m) wavelengths due to k fluorophores is defined according to Equation (2):

$$F(\lambda_x, \lambda_m) = P_0(\lambda_x) \int_0^L dz\, \Omega \sum_{k=1}^{N} \mu_{a_k}(\lambda_x)\phi_k(\lambda_m) \quad (2)$$

and Equation (3) gives the definition of $\mu_a(\lambda_x)$, the absorption coefficient of the fluorophore at the excitation wavelength:

$$\mu_a(\lambda_x) = 2.303\varepsilon(\lambda_x)C \quad (3)$$

In Equations (2) and (3) $\phi(\lambda_m)$ is the quantum yield of the fluorophore at the emission wavelength, $P_0(\lambda_x)$ is the power of the intensity at the excitation wavelength, L is the path length and Ω is the detector collection efficiency. The absorption coefficient $\mu_a(\lambda_x)$ is a linear function of $\varepsilon(\lambda_x)$ and C, which are the extinction coefficients at

excitation wavelength and concentration, respectively, of the fluorophore. Although fluorescence spectroscopy of optically dilute, homogeneous media is well understood, fluorescence spectroscopy of turbid media, such as human tissue, is complicated by its highly absorbing and scattering properties.[53]

3.2 Fluorescence Spectroscopy of Turbid Media such as Tissue

Fluorescence spectroscopy of turbid media such as tissue depends on one or more of the following. Specifically, it depends on the concentration and distribution of fluorophore(s) present in the tissue as well as the biochemical/biophysical environment, which may alter the quantum yield and lifetime of the fluorophore(s). For example, epithelial tissues generally have two primary sublayers – a surface epithelium and an underlying stroma or submucosa; the specific fluorophores, as well as their concentration and distribution, can vary significantly between these two tissue layers. Fluorescence spectroscopy of turbid media such as tissue also depends on the absorption and scattering that result from the concentration and distribution of nonfluorescent absorbers and scatterers, respectively, within the different sublayers of the tissue.

The effect of the aforementioned variables on fluorescence spectroscopy of tissue is wavelength dependent. First, the endogenous fluorophores that have absorption bands that lie in the same wavelength range as the excitation light will be excited and hence will emit fluorescence. The absorption and scattering properties of the tissue will affect light at both of these excitation and emission wavelengths. Therefore only those fluorophores contained in the tissue layers to which the excitation light penetrates and from which the emitted light can escape the tissue surface will produce measurable fluorescence. Elastic scattering events in tissue are caused by random spatial variations in the density, refractive index and dielectric constants of extracellular, cellular and subcellular components.[54] Tissue scattering generally decreases monotonically with increasing wavelength over the UV, VIS and NIR spectral regions.[11] Tissues are generally forward scattering (mean anisotropy factor is between 0.97 and 0.98), with scattering coefficients ranging from 10 to $1000\,cm^{-1}$ from the NIR to the UV spectral range.[11] Absorption in tissue in the UV, VIS and NIR regions is primarily attributed to hemoglobin.[55] Although absorption in tissue is strongly wavelength dependent, it tends to decrease generally with increasing wavelengths.[11] Typically, tissue absorption coefficients range from 0.1 to $10\,000\,cm^{-1}$ from the NIR to the UV spectral range. Consequently, the penetration depth of light, which is primarily a function of the tissue absorption properties,

decreases from several centimeters to a few hundred microns from the NIR to the UV.[11] For example, in the UV spectral region, the penetration depth of light in tissue is approximately 225 µm at 337 nm.[3]

Hemoglobin, which is contained in red blood cells, serves as the oxygen carrier in blood and also plays a vital role in the transport of carbon dioxide and
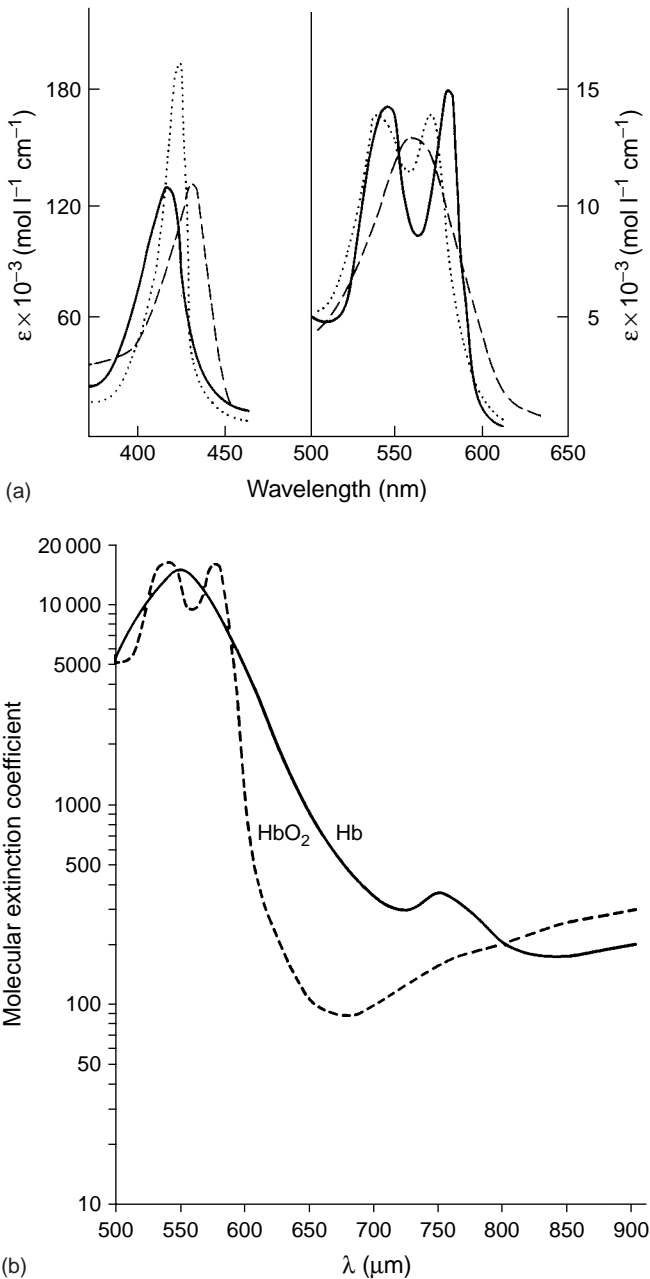

(a)

(b)

Figure 6 Absorption spectra of oxygenated and deoxygenated hemoglobin over: (a) UV/VIS spectral region (solid line, HbO$_2$; dashed line, Hb; dotted line, Soret band); (b) NIR spectral region. (Reproduced by permission of Academic Press, Orlando, Florida, from Brown.[55])

hydrogen ions.[40] The capacity of hemoglobin to bind oxygen depends on the presence of a nonpolypeptide unit, namely a heme group. The heme consists of an organic part, a protoporphyrin ring and an iron atom. Figure 6 displays the absorption spectra of oxygenated and deoxygenated hemoglobin over the UV/VIS (Figure 6a) and NIR (Figure 6b) spectral regions.[55] In Figure 6(a), the absorption spectra are characterized by the Soret band at 400–450 nm, the bands at 540 (α band) and 569 nm (β band) of oxygenated hemoglobin and the 557 nm band of deoxygenated hemoglobin. In Figure 6(b), the absorption spectra are characterized by the decreasing absorption of deoxygenated hemoglobin and the increasing absorption of oxygenated hemoglobin as a function of increasing wavelength.

The effect of hemoglobin absorption is noticeable when comparing fluorescence emission spectra measured from an optically thick arterial tissue sample (250 µm thickness) to that measured from a corresponding, optically thin tissue section (4 µm thickness) using the same illumination and collection geometry, as shown in Figure 7.[56] Evaluation of Figure 7 indicates that the fluorescence intensity of the optically thick tissue sample is significantly reduced and, furthermore, its line shape is characterized by a valley at 420 nm, which corresponds to the Soret absorption band of hemoglobin.[55] The fluorescence emission spectrum of the optically thin tissue section may be attributed to collagen fluorescence.

The illumination and collection geometry of the excitation and the emitted light, respectively, can also affect fluorescence measurements from tissue with respect to both the intensity and line shape.[54,57,58] This may be attributed to the fact that although fluorescence is generated isotropically from the fluorophores within the
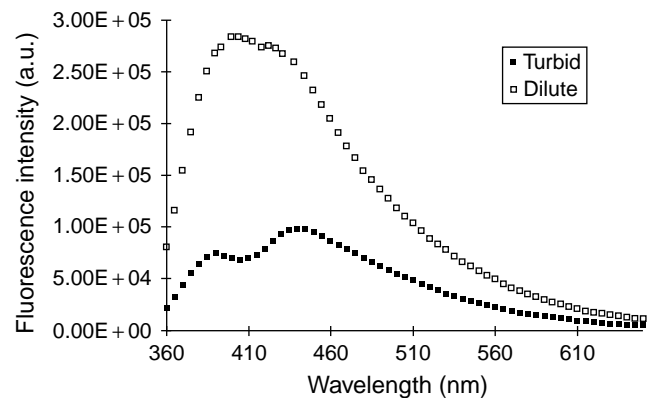

Figure 7 Fluorescence emission spectra at 340 nm excitation, measured from an optically thick, arterial tissue sample (250 µm thickness) to that measured from a corresponding, optically thin, tissue section (4 µm thickness) using the same excitation and collection geometry. (Reproduced by permission of the Optical Society of America, from Durkin et al.[56])

biological medium, the fluorescence emitted from the surface of the medium may range from isotropic to anisotropic, depending on whether the medium is highly absorbing, dilute or turbid.[54] Monte-Carlo simulations have been used extensively to simulate light distribution in turbid media to explore the effect of absorption and scattering on the fluorescence emitted from the surface of tissues using finite excitation beam profiles and complex excitation and emission geometries.[57] The results of these simulations indicate several important findings.

The profile of the excitation beam greatly affects the distribution of the excitation light in the tissue and thus is an important factor. For a Gaussian beam profile, the fluorescence distribution at a specific emission wavelength on the surface of the tissue is peaked and narrow, whereas for a uniform profile it is wider and less peaked. Furthermore, the effect of absorption, particularly due to hemoglobin, on the measured fluorescence increases as the collection fiber is moved further away from the illumination fiber on the surface of the tissue, resulting in decreased fluorescence intensity. In addition, the effect of this absorption is wavelength dependent, suggesting that it will affect the line shape of the fluorescence as well. This is evident when comparing the fluorescence emitted at two wavelengths at which hemoglobin has different absorption characteristics. As the distance of the collection fiber increases relative to the illumination fiber, the ratio of the fluorescence intensity at the two emission wavelengths deviates from unity. This suggests that collecting the emitted light from the tissue site directly illuminated by the excitation light will minimize the distortion due to hemoglobin absorption, albeit this will reduce the sampling depth for the fluorescence measurements.

The effect of the illumination and collection geometry on fluorescence measurements from tissue is illustrated in Figure 8, which displays the fluorescence emission spectra at 476 nm excitation of normal human cadaver aorta (N) and of one with atheromatous plaque (P).[58] In Figure 8(a) fluorescence was collected from the tissue site directly illuminated by the excitation light, and in Figure 8(b) the fluorescence was collected from a circular area around the directly illuminated area. Both the intensity and line shape of the fluorescence are affected by the probe geometry. For the normal aorta (Figure 8a) the ratio of the fluorescence intensity at 600 and 580 nm is 1.27, whereas it is 1.72 in Figure 8(b). For the atheromatous tissue, the ratio is 0.91 for both collection areas.

3.3 Deconvolution of Absorption and Scattering from Tissue Fluorescence Emission Spectra

Fluorescence excitation and emission from turbid media such as tissues consist of three components: the distribution of the excitation light in the tissue, which is a function of the absorption and scattering coefficients of the medium at that wavelength; the fluorescence of isotropically radiating point sources located at different depths within the tissue, which is determined by the fluorescence quantum yield of the fluorophore and the excitation intensity at that depth; and the total fluorescence escaping the surface of the tissue, which is a function of the absorption and scattering properties of the medium at that wavelength. Quantification of the concentration of fluorophores within tissue in principle involves deconvoluting the absorption and scattering properties of the tissue from the measured fluorescence emission spectrum and quantifying the identity and distribution of the fluorophores that contribute to the deconvolved spectrum. The former requires the development of a transfer function based on the measurements of tissue optical properties, i.e. the absorption and scattering coefficients and the anisotropy parameter, whereas the latter requires knowledge of the identity and distribution of the fluorophores within the tissue.

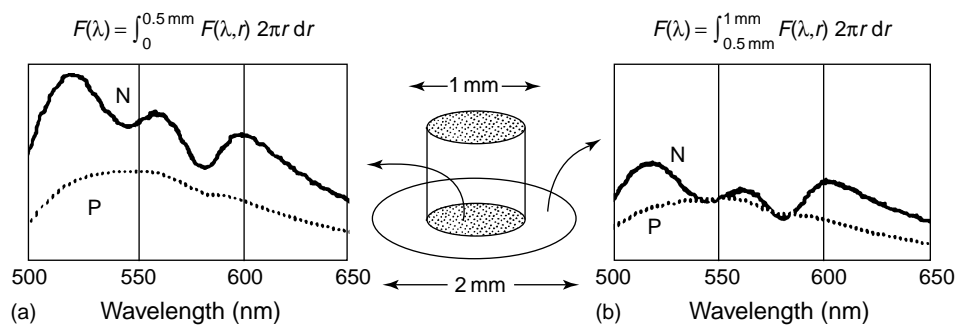**Figure 8** Fluorescence emission spectra at 476 nm excitation of normal human cadaver aorta (N) and one with atheromatous plaque (P): (a) the fluorescence was measured from the tissue site directly illuminated by the excitation light; (b) the fluorescence was measured from a circular area around the directly illuminated area. (Reproduced by permission of the Optical Society of America, from Keijzer et al.[58])

For a turbid medium such as tissue that contains k fluorophores, the fluorescence intensity can be rewritten to include a transfer function (TF) that describes the attenuation of the excited and emitted light due to the absorption and scattering properties of the tissue at these wavelengths.[54] This is defined in Equation (4):

$$F(\lambda_\mathrm{x}, \lambda_\mathrm{m}) = P_0(\lambda_\mathrm{x}) \int_0^\infty \mathrm{d}z \sum_{k=1}^N \mu_{\mathrm{a}_k}(\lambda_\mathrm{x}, z)\phi_k(\lambda_\mathrm{m}, z)$$
$$\times\, TF(\lambda_\mathrm{x}, \lambda_\mathrm{m}, z)\Omega \quad (4)$$

where z refers to the depth within the medium. Here, the transfer function for a particular depth can be determined from the tissue absorption coefficient, the scattering coefficient and the anisotropy factor. The wavelength-dependent absorption coefficient (μ_a) denotes the probability of photon absorption per unit path length, whereas the scattering coefficient (μ_s) denotes the probability of photon scattering per unit path length. The anisotropy factor (g) denotes the cosine of the average scattering angle. The reduced or isotropic scattering coefficient (μ_s') is the product of the scattering coefficient (μ_s) and one minus the anisotropy parameter ($1 - g$). Models of light transport[59–65] can be used to deduce the absorption and scattering coefficients and the anisotropy parameter needed to compute the transfer function in Equation (4).

3.3.1 Models of Light Transport

Most models of light transport used to quantify tissue optical properties to date have been either numerical or approximate analytical solutions of the neutral particle transport equation.[59,60] Because of the inhomogeneity of tissues, the solution of Maxwell's equations, which might otherwise be used to model light propagation in tissues, is generally not feasible. However, if polarization and diffraction effects are ignored, the transport of photons through random media may be modeled as neutral particle transport. The neutral particle transport theory is heuristic and is based on a statistical approximation of photon transport in a multiple-scattering medium. Within this framework, the propagation of light is described in terms of the transport of discrete photons, which may be either scattered or absorbed. The transport equation (Equation 5) is defined as:

$$\frac{1}{c}\frac{\partial\phi(\vec{r}, \widehat{\Omega})}{\partial t} + \widehat{\Omega} \bullet \nabla\phi(\vec{r}, \widehat{\Omega}) + [\mu_\mathrm{a}(\vec{r}) + \mu_\mathrm{s}(\vec{r})]\phi(\vec{r}, \widehat{\Omega})$$
$$= \mu_\mathrm{s}(\vec{r}) \int_{4\pi} \mathrm{d}\widehat{\Omega}' f(\widehat{\Omega}' \to \widehat{\Omega})\phi(\vec{r}, \widehat{\Omega}') + s(\vec{r}, \widehat{\Omega}) \quad (5)$$

where $\phi(\vec{r}, \widehat{\Omega})$ is the local angular flux of photons at position $\vec{r}$, angle $\widehat{\Omega}$ and time t in a scattering medium. The absorption coefficient $\mu_\mathrm{a}(\vec{r})$ describes photon absorption

at position $\vec{r}$, and the scattering coefficient $\mu_\mathrm{s}(\vec{r})$ describes photon scattering at position $\vec{r}$. The term $f(\widehat{\Omega}' \to \widehat{\Omega})$ is the scattering phase function, which describes the probability of a photon scattered from direction $\widehat{\Omega}'$ into direction $\widehat{\Omega}$. Term $S(\vec{r}, \widehat{\Omega})$ is a source term for photons at position $\vec{r}$ and angle $\widehat{\Omega}$. Equation (5) can be solved numerically or approximated analytically to determine the position- and angle-dependent flux of photons in a medium described by an arbitrary absorption, scattering and phase function distribution.

Approximate analytical models include the following approximations. The simplest analytical model is the Beer–Lambert law,[2] which assumes that the incident light on the medium attenuates exponentially in the direction of propagation within that medium. This is valid for a medium that does not scatter light, but is sufficiently absorbing that it can no longer be dilute, which is generally not true for tissues. The Kubelka–Munk approximation[61] describes the time-independent, diffuse reflectance and transmittance for light incident on a tissue slab in terms of its spatially uniform absorption and isotropic scattering coefficients. The radiative transport equation also can be solved using the adding–doubling method[62] for appropriate boundary conditions, and its solution can be compared with measurements of time-independent, diffusely reflected and transmitted light to estimate the absorption and scattering, as well as the anisotropy factors. Models based on Kubelka–Munk and the adding–doubling method are appropriate for the determination of tissue absorption and scattering coefficients in a wavelength region in which neither absorption nor scattering in tissue is dominant (UV/VIS spectral regions).

Within the diffusion approximation,[63] which is valid far from sources and when the scattering coefficient is several orders of magnitude greater than the absorption coefficient, the spatial and temporal distribution of the diffusely reflected or transmitted light from tissue is related to the absorption and scattering coefficients and anisotropy factor. Diffusion theory is valid for cases where the absorption is low and scattering is high in tissues, such that the light is multiply scattered and travels through various optical path lengths before being detected (as in the NIR spectral region). When the probability of absorption in tissue becomes significant (as in the UV/VIS spectral regions), re-emitted light is minimally or moderately scattered and diffusion theory is no longer valid.

Numerical solutions to the transport equation include the method of discrete ordinates[64] and the Monte-Carlo technique.[65] These techniques can be used to model light transport in tissue over the entire UV/VIS/NIR spectral regions. The Monte-Carlo technique, which has been the

more popular of these numerical models, tracks individual photon trajectories, which are computer-simulated to calculate absorption and scattering coefficients (inverse calculation) or space irradiance distributions (forward calculation) for any tissue, tissue geometry and wavelength region. However, because tens of millions of photon trajectories must be tracked for statistical simulation of light transport in tissue, computations are time intensive.

The aforementioned numerical techniques can be used to compute the absorption and scattering coefficients and anisotropy parameter from measurements of diffusely reflected and transmitted light from tissue. Additionally, if the optical properties are known at the specific excitation and emission wavelengths and the fluorophore(s) quantum yield and distributions are provided, fluorescence excitation, emission and escape from the different depths within the tissue can be computed. Hence, these numerical techniques can be used to compute numerically the transfer function in Equation (4).

3.4 Turbid Tissue-simulating Phantoms for Fluorescence Spectroscopy of Tissue

In order to evaluate the effect of absorption and scattering and the illumination and collection geometry experimentally on fluorescence measurements from tissue, it is useful to employ tissue phantoms that simulate the optical properties and fluorescent properties of these biological media.

Durkin et al.[66] developed a liquid tissue phantom that simulates the optical and fluorescence properties of tissues over the range 350–650 nm, with absorption coefficients in the range 25–5 cm^{-1}, scattering coefficients, in the range 400–200 cm^{-1} and fluorophores in the micromolar concentration range. Phantom fluorophores included FAD and rhodamine B. Absorption was controlled by adjusting the hemoglobin concentration. Polystyrene spheres, which have a smoothly varying scattering coefficient as a function of wavelength, were used as the scatterers. Sample inhomogeneities were simulated by preparing the phantom in a gelatin substrate. These phantoms could be made dilute, absorbing and/or turbid.

Wagnieres et al.[67] also developed tissue phantoms that have the optical characteristics of biological tissues in the wavelength range 400–650 nm, with absorption coefficients in the range 21–0.7 cm^{-1} and scattering coefficients in the range 680–220 cm^{-1}. The phantoms are made up of agarose dissolved in water to provide a transparent matrix, which is then loaded with silicon dioxide, Intralipid, ink, blood, azide, penicillin, bovine serum and fluorophores. The silicon dioxide and Intralipid particles are responsible for scattering, whereas the ink and blood are absorbers. The penicillin and azide

are used to ensure conservation of the phantoms at 4 °C. The serum, and fluorophores such as Coumarin 30, produce fluorescence. The mechanical properties of these gelatinous phantoms render them easily moldable so that complex structures and shapes simulating layered or other inhomogeneous structures containing various amounts of absorber, scatterer and fluorophore can be developed.

4 INSTRUMENTATION

In order to perform quantitative fluorescence spectroscopy of tissue, the fluorescence emission spectra and the reflectance and/or the diffuse reflectance and transmittance need to be measured. The latter are needed if tissue optical properties are to be quantified. However, because intact issues are semi-infinite media, only fluorescence emission and reflectance spectra are measured from these biological systems.

A schematic of the basic components of an instrument used for fluorescence and/or reflectance spectroscopy of tissues is shown in Figure 9. It consists of a light source, a flexible, conduit that contains optical fibers for the illumination and collection of light, a dispersing element that separates the emitted light into its respective wavelengths, and a detector that measures the intensity at these wavelength(s). In this scenario, fluorescence emission and reflectance are measured in a re-emission geometry in which the illumination and collection are performed on the same surface of the tissue. The various types of instruments employed for these measurements essentially have the same basic components.

4.1 Light Sources

Lasers, which have a very narrow spectral output, are generally used as monochromatic excitation light sources for fluorescence spectroscopy, whereas lamps with a broad spectral output are more appropriate for
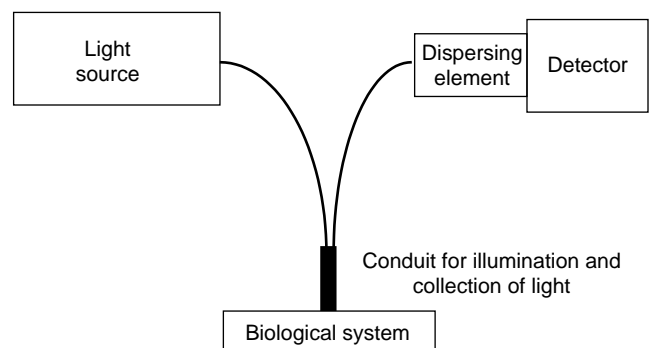

Figure 9 Schematic drawing of a fiber-optic-based instrument for fluorescence and/or reflectance spectroscopy.

reflectance spectroscopy. Lamps also can be used as quasi-monochromatic excitation light sources for fluorescence spectroscopy when coupled with a monochromator or narrow-bandpass filter (see section 4.3). The need for portable light sources for clinical applications has limited the use of monochromatic light sources in the UV/VIS spectral range to the nitrogen pumped-dye laser (fundamental wavelength is 337 nm) and the helium–cadmium laser (wavelengths are 325 and 442 nm). Additionally, a dye module coupled to the nitrogen laser enables the generation of VIS laser wavelengths through the use of appropriate chemical dyes in a resonant cavity. Other lasers that have been used for fluorescence spectroscopy include the argon ion (UV and blue), helium neon (red) and krypton ion (blue) lasers. Portable polychromatic sources include the mercury and xenon arc lamps. The primary criteria for the selection of light sources, in addition to portability, are output power, bandwidth, wavelength tunability, coupling efficiency (into optical fibers) and the need for pulsed versus continuous wave light sources.

The power from a portable nitrogen laser at 337 nm is ∼300 µJ per pulse. At a maximal repetition rate of 30 Hz its average power is ∼9 mW. Because the nominal conversion efficiency of dyes used to generate VIS wavelengths is approximately 10%, the average power in this case would be ∼1 mW. The output power from the helium–cadmium laser ranges from 5 mW at 325 nm to 15 mW at 442 nm. Commercially available mercury and xenon arc lamps can be operated over a range of 50–1000 W. Owing to excess generation of heat in the IR, clinical applications employing these lamps have been restricted to the use of power supplies between 75 and 300 W, with a liquid filter for IR rejection. Note that the output powers available for tissue illumination are significantly lower than the output powers specified, due to coupling losses from the light source into the optical fibers and/or coupling optics.

Although the UV/VIS lasers afford a very narrow spectral band (1–2 nm), the bandwidth of illumination from a lamp is determined by the use of narrow-bandpass filters or a monochromator (see section 4.3), which is used for wavelength dispersion. In general a 10–20 nm bandpass for the light source is sufficient, because tissue fluorescence emission spectra are broad with a 40–60 nm full width at half-maximum (fwhm).

The advantages and disadvantages of using a lamp versus a laser for fluorescence spectroscopy should be considered. An advantage of using a mercury or xenon lamp over a laser is that it provides wavelength tunability over the UV/VIS spectral range, as shown in Figure 10.[68] However, the disadvantage of using a lamp over a laser is that the coupling efficiency into optical fibers can be reduced by a factor of 20 compared to laser coupling,[69] due to the relatively large focal
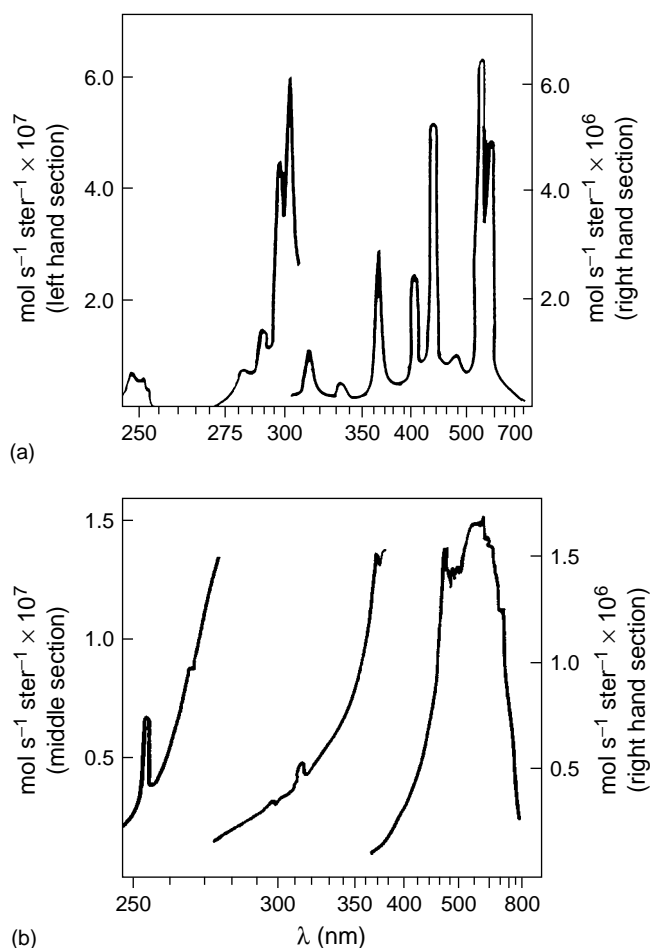
Figure 10 Typical radiant intensity and shape of the emission spectra of: (a) mercury lamp; (b) xenon arc lamp. (Reproduced by permission of Academic Press, Orlando, Florida, from Kohen et al.[68])

spot diameter of arc lamps. Finally, lasers with very short pulse duration (of the order of nanoseconds) are necessary when the tissue needs to be illuminated with pulsed excitation light for gated detection (which provides effective rejection of ambient light during fluorescence measurements) and for fluorescence lifetime measurements.

4.2 Illumination and Collection of Light

With respect to illumination and collection of light from tissue, two different approaches may be considered: the contact approach, where fiber-optic probes are placed directly in contact with the tissue surface; and the noncontact approach, where a series of lenses are used to project the light onto the tissue surface and collect it in a similar manner. With the contact approach, variable pressure on the tissue may distort the signal. However, with the noncontact approach the signal strength will vary

with the source–tissue and tissue–detector distances. In general, the contact approach is used for steady-state and time-resolved fluorescence and reflectance spectroscopy from small tissue volumes, whereas the noncontact approach is more suited for imaging larger tissue areas.

For the fiber-optic-based approach, typically multi-mode, step-index fibers with a core diameter ranging from 100 µm to 1 mm and f numbers (see section 4.3) of 2–4 are used for UV/VIS, fluorescence and reflectance spectroscopy. Fused-silica optical fibers are used for UV-excited fluorescence spectroscopy because standard silica fibers generate fluorescence with UV excitation.

The fluorescence emission spectra of turbid media such as tissue are extremely dependent on the illumination and collection geometry due to the interaction of absorption and fluorescence.[57] As shown elsewhere,[57,58] design of a fiber-optic probe configuration that reduces the distortion of the fluorescence emission spectrum due to tissue absorption consists of a geometry in which the tissue fluorescence is collected only from that surface directly illuminated by the excitation light. Richards-Kortum et al.[57] first designed optical fiber probes with illumination and collection geometries that enable maximal overlap between excitation and emission areas on the tissue surface.

In general, reflectance spectroscopy refers to the detection of both the diffuse (multiply scattered) and specular (surface) components of the reflectance. When measuring the diffuse reflectance from tissues, the photons that are detected generally undergo multiple scattering events and the photon path lengths are much greater than the geometric separation between the source and detector. Consequently, through this measurement, the probe is able to sample features in the tissue volume. Because specular reflection is due to refractive index mismatch and is generally a 2% reflection of the incident light in the case of an air/tissue interface, it needs to be minimized in attempting to make diffuse reflectance measurements. In order to minimize specular reflection, geometries have been employed in which the source and detector fiber are placed adjacent to each other, so that the specularly reflected light is not coupled to the detector fiber.[9] However, this geometry precludes the ability to collect diffuse reflectance from the same site that is illuminated. This presents two problems: there is attenuation of the signal; and if fluorescence measurements are made from the same site of illumination there will be a lack of congruence between the fluorescence and reflectance measurements. One way to minimize specular reflection in a case where the diffuse reflectance is collected from the same site that is illuminated is to have the distal tip of the collection fiber angled at 17° from the direction normal to the optical fiber axis, such that the specular reflection is not coupled but the diffuse reflectance is.[69]

4.3 Monochromators and Spectrographs

Light can be dispersed spectrally using a monochromator or a spectrograph, which are both dispersing components. A monochromator presents one wavelength or bandpass at a time of the input light from its exit slit, whereas a spectrograph presents a range of wavelengths simultaneously at the exit focal plane. Monochromators can be used as filters in conjunction with arc lamps to produce a series of monochromatic outputs for sample illumination (if only a few wavelengths are needed, narrow-bandpass filters may be more appropriate) or can be used to disperse the emitted light into its respective wavelengths, each of which can be detected serially using a single-channel detector. Spectrographs can used to disperse the emitted light into its respective wavelengths simultaneously for multichannel detection.

The key components of a monochromator/spectrograph are: an entrance slit; a collimating lens; a grating (dispersing unit) for wavelength selection; a focusing lens; and an exit slit (see Figure 11). Grooves in diffraction gratings are manufactured either classically with the use of a ruling engine (ruled gratings) or holographically with the use of interference fringes generated at the intersection of two laser beams (holographic gratings). Groove densities generally range from 50 to 3600 grooves mm^{-1}. Holographic gratings have a higher groove density than ruled gratings.

Parameters that are relevant to the selection of a monochromator/spectrograph are the reciprocal linear dispersion (mm nm^{-1}), transmission efficiency, f number and stray light rejection. The reciprocal linear dispersion (which is inversely related to the grating groove density, diffraction order and focal length of the focusing element), when multiplied by the entrance slit width, provides the spectral resolution. For fluorescence and
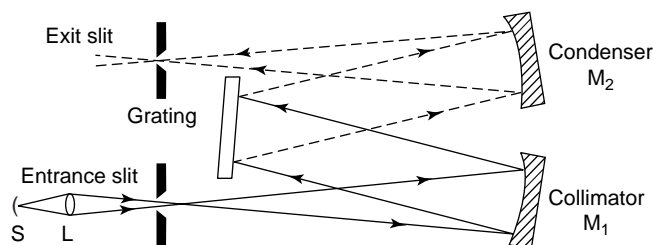

Figure 11 Schematic drawing of a monochromator that shows the arrangement of the light source (S), the condensing lens (L), the entrance slit, the mirror optics (M$_1$ and M$_2$), the grating and the exit slit. (Reproduced by permission of Academic Press, Orlando, Florida, from Kohen et al.[68])

reflectance spectroscopy, generally a spectral resolution of 10 nm is sufficient because these spectra are broad band and hence lack structure within this bandpass. Transmission efficiencies of both holographic and ruled gratings are comparable (~40%) in the VIS spectral region, and the efficiency of a particular grating is maximal at the wavelength at which it is blazed. Collection efficiency is reflected by the f number, which is defined as the ratio of the focal length and diameter of the collimating element. Lower f numbers are usually associated with a higher light gathering power or throughput. However, higher f-number spectrographs with longer focal-length-collimating elements are generally used to project a wide, flat field ideal for multichannel imaging detectors. For the applications indicated here, generally f numbers that match those of standard optical fibers (~2–4) are selected in order to maximize coupling efficiency. Stray light in monochromators/spectrographs is due to diffusion of light by optical components, including gratings and mirrors. Stray light is reduced by using holographic gratings, which usually give an order of magnitude better stray light rejection than classically ruled gratings. Typical stray light rejection for UV/VIS, fluorescence and reflectance spectroscopy should be specified to five orders of magnitude lower than the signal. Otherwise, long-pass filters with an optical density of at least 5.0 at the wavelength of excitation have to be employed to block the excitation light from the detector.

4.4 Detectors

The important considerations in choosing a detector are the type of measurements being made, i.e. single wavelength versus multiwavelength and single pixel (small region of the tissue surface) versus multipixel (relatively larger tissue area). Fluorescence and reflectance measurements from single pixels can be made either using a single-channel or multichannel detector. If measurements at only one or several wavelengths are being made, a single-channel photoemissive tube – called a photomultiplier tube (PMT) – or a semiconductor-based avalanche photodiode (APD) with a bandpass filter can be used. For fluorescence or reflectance spectroscopy, a spectrograph coupled to a multichannel, linear photodiode array (PDA) is appropriate. Fluorescence and reflectance spectroscopy also can be performed using a monochromator coupled to a PMT, albeit this substantially increases the measurement time. In the case of measurements from multiple pixels on the tissue surface, a two-dimensional charge-coupled device (CCD) camera may be employed. In order to reduce or eliminate the detection of ambient light during fluorescence spectroscopy, a detector with an intensifier for fast gating (several nanoseconds) must be used in conjunction with a pulsed excitation light source.

With respect to general detector performance, other considerations include quantum efficiency and sources of noise. For the detector, the quantum efficiency is defined as the ratio of induced current to the induced flux (often measured in electrons per photon). The quantum efficiency depends on the wavelength of light used, the material type and shape and other physical parameters. Figure 12 displays the quantum efficiency of a PMT and PDA/CCD.[70]

The noise components that we must consider when detecting light are as follows:

- Shot noise, which is due to random statistical fluctuations of the incident light. Shot noise increases with the square root of the signal.
- Dark signal, which comes from the random generation of electrons. Dark signal is temperature dependent and thus can be reduced by cooling the detector.
- Readout noise, which comes from the electronic process of reading the signal from the detector.

The dark flux for a PMT lies in the range $2-50 \, e^- \, s^{-1}$. The readout noise is essentially zero because the pulse-height discrimination effectively avoids quantization noise. Although the un-intensified PDAs have been applied where the light levels are high, as in the case of reflectance spectroscopy, intensified PDAs are more suitable for fluorescence spectroscopy in which light levels are several orders of magnitude lower. In an intensified PDA, a microchannel plate intensifier is used to amplify the photoelectrons by a factor of 3000. Typical dark (at $-20\,^\circ C$) and readout noises are $40 \, counts \, s^{-1}$ and $3 \, e^-$, respectively (manufacturer specification is 1 count per e^-). The dark current of the CCD cameras range from $12 \, e^- \, pixel^{-1} \, s^{-1}$ at $-40\,^\circ C$ to $0 \, e^- \, pixel^{-1} \, s^{-1}$ when cooled to $-110\,^\circ C$. Their readout noise ranges from 12 to $4 \, e^-$.
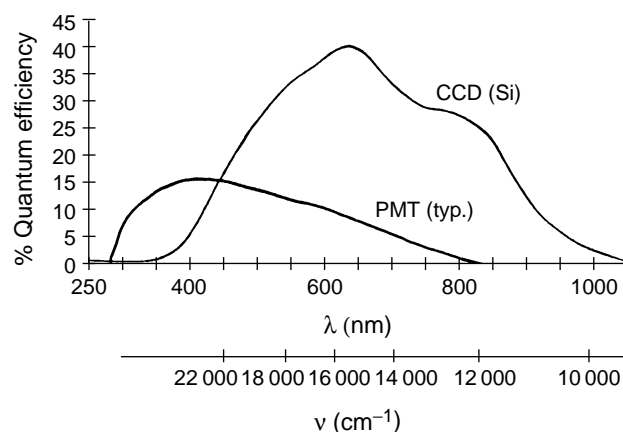

Figure 12 Quantum efficiency of a PMT and PDA/CCD.

4.5 Signal-to-noise Ratio Analysis of an Instrument Used for Fluorescence Spectroscopy of Tissue

To establish the performance of an instrument for fluorescence spectroscopy of tissue (fluorescence rather than reflectance measurements are limiting in signal to noise), Zangaro et al.[69] did a signal-to-noise ratio analysis using typical components. They used a nitrogen pumped-dye laser coupled to a fiber-optic probe for illumination and collection, and a spectrograph coupled to an intensified PDA for detection. Their calculation is as follows. The output pulse energy of the nitrogen laser is ~300 μJ. If the dye module is used, the nominal conversion efficiency is around 10%, but with surface reflection losses it becomes 25 μJ per pulse. They calculated losses of 40% in coupling this light to a 200-μm core diameter fiber, resulting in an output energy of 16 μJ per pulse. Assuming a tissue fluorescence efficiency in the 400-nm region to be 0.01%, the average fluorescence energy that they calculated is ~1.6 nJ. Given a collection efficiency of 1% of the fluorescence escaping from the tissue surface to the detector fiber, the fluorescence energy coupled to the detector fiber is ~16 pJ. Accounting for coupling losses and transmission efficiency through the spectrograph, the total energy pulse that reaches the PDA is two orders of magnitude lower, i.e. 400 fJ.

The signal-to-noise ratio obtainable by the PDA is determined by S, which is the total number of photoelectrons that reach the detector, and N, which is the number of photoelectrons associated with noise. The total noise generated by the various sources is defined according to Equation (6):

$$N = (S + N_R^2 + N_D^2)^{1/2} \tag{6}$$

where the square root of S is the shot noise from the signal photoelectrons collected by the detector, N_R is the read-out noise inherent in the amplifier and electronics and N_D is the noise due to the dark current and is dependent on the exposure time and temperature. Because the detector is Peltier cooled to 5 °C during operation, the dark current is negligible. The signal that reaches the photodetector is estimated to be 400 fJ. Given a quantum efficiency in the 400-nm region of 50% (1×10^{18} photoelectrons J^{-1}), approximately 400 000 photoelectrons reach the PDA. The shot noise is calculated to be 632 electrons. The read-out noise for the PDA is 3000 electrons. Using these quantities, the signal-to-noise ratio obtainable with these parameters is approximately 130. Trujillo et al. have also done a systematic evaluation of the signal-to-noise ratio of a typical instrument used for fluorescence spectroscopy of tissue.[71] In addition, they have developed an analytical expression to quantify the fluorescence efficiency of the tissue, which they have incorporated into the signal-to-noise ratio analysis of their fluorimeter.

4.6 Calculation of Tissue Fluorescence Efficiency

In order to calculate the expected signal-to-noise ratio of a fluorimeter, two quantities are required: the throughput and inherent noise of the fluorimeter; and the fluorescence efficiency of the tissue volume probed. The throughput and inherent noise of the fluorimeter is a function of the delivery of the excitation light to the tissue surface, the collection of the fluorescence from the tissue surface, and finally conversion of the optical signal to an electronic signal. The calculation of these three quantities has been described in section 4.5. The fluorescence efficiency is the quantitative relationship between the excitation and emission energy. Trujillo et al.[71] have developed an analytical expression to calculate the fluorescence efficiency of tissue from fluorescence emission spectra of tissues measured in vivo.

The fluorescence efficiency (*FE*) of a turbid sample is defined as the ratio of the total emitted photons to the excitation photons and is described as shown in Equation (7):

$$FE = \int_0^\infty dz \int_{\lambda_m}^\infty d\lambda_m H_{in}(\lambda_x, z) \sum_k [\mu_{a_k}(\lambda_x, z)$$
$$\times \phi_k(\lambda_m, z)] H_{out}(\lambda_m, z) \tag{7}$$

where λ_x is the excitation wavelength, λ_m is the emission wavelength, z is the depth within the sample, $\mu_a(\lambda_x, z)$ represents the absorption coefficient at the excitation wavelength of the fluorophore at depth z, $\phi(\lambda_m, z)$ is the fraction of the absorbed energy converted to fluorescence at the emission wavelength of the fluorophore at depth z, and $H_{in}(\lambda_x, z)$ and $H_{out}(\lambda_m, z)$ represent the attenuation of the excitation and emission light, respectively, at depth z. The fluorescence efficiency is independent of the power of the intensity at the excitation wavelength and the illumination/collection geometry. The fluorescence efficiency of an unknown turbid sample can be calculated from fluorescence measurements of the unknown sample and fluorescence measurements of an optically dilute homogeneous standard with a known absorption coefficient (μ_a) and quantum efficiency using the same apparatus. Given the fluorescence emission spectrum of the turbid sample and that of a homogeneous standard with a known μ_a and quantum efficiency, the fluorescence efficiency of the turbid sample can be expressed by Equation (8):

$$FE_t(\lambda_x, \lambda_m) = \left[\frac{\int_{\lambda_m}^\infty P_t(\lambda_x, \lambda_m) d\lambda_m}{\int_{\lambda_m}^l P_{std}(\lambda_x, \lambda_m) d\lambda_m} \right] \times$$

$$\left[\frac{\int_0^l dz \int_{\lambda_m}^\infty d\lambda_m H_{in-std}(\lambda_x, z) \mu_{a-std}}{\times (\lambda_x) \phi_{std}(\lambda_m) H_{out-std}(\lambda_m, z) \Omega_t} \right] \tag{8}$$

where the subscript "t" corresponds to that of the turbid sample, the subscript "std" corresponds to that of the homogeneous standard, P_t is the total integrated fluorescence power of the turbid sample, P_{std} is the total integrated fluorescence power of the homogeneous standard (both of which can be measured), and Ω_t and Ω_{std} represent the collection efficiency of the turbid sample and homogeneous standard respectively. The first term in Equation (8) can be calculated from the ratio of the total integrated fluorescence power of the turbid sample and the homogeneous standard. The second term requires knowledge of the optical properties as well as the collection geometry of the homogeneous standard. The authors used a rhodamine solution in a cuvette as the homogeneous standard in these calculations. Because the rhodamine standard used is an optically dilute homogeneous solution, and the numerical aperture of the excitation and collection is small (0.22), the attenuation of the excitation light and fluorescent light in the rhodamine standard can be described with the simple Beer–Lambert Law.[2] Hence, the wavelength-dependent μ_a can be calculated simply from the measured rhodamine absorbance. The quantum efficiency of rhodamine is unity.[72] The double integral in Equation (8) can be evaluated by using the measured values of $\mu_a(\lambda_x)$, $\mu_a(\lambda_m)$ and $\phi(\lambda_m)$ of the homogeneous standard. If $\phi(\lambda_m)$ is not known but the quantum efficiency is, then an alternative method can be used to calculate the fluorescence efficiency, which requires changing $\phi(\lambda_m)$ into the quantum efficiency QE (defined by Equation 9):

$$QE = \int_{\lambda_x}^{\infty} d\lambda_m \phi(\lambda_m) \qquad (9)$$

Figure 13 displays the average fluorescence efficiency calculated from the fluorescence emission spectra of a total of 374 human cervical tissues at three excitation wavelengths in vivo. In Figure 13, the average fluorescence efficiency values are plotted for normal squamous tissue, normal columnar tissues, low-grade squamous intra-epithelial lesions (SIL) and high-grade SIL at excitation wavelengths 337, 380 and 460 nm. Standard deviations are shown as error bars. For squamous cervical tissues, the fluorescence efficiency decreases as tissue progresses from a nondiseased normal squamous to a diseased state (low-grade and high-grade SIL). Furthermore, as the excitation wavelength increases, the fluorescence efficiency decreases. The fluorescence efficiencies shown here are instrument independent and can be used to determine the signal-to-noise ratio needed to measure fluorescence emission spectra from tissues for different instrument configurations and excitation–emission collection geometries.
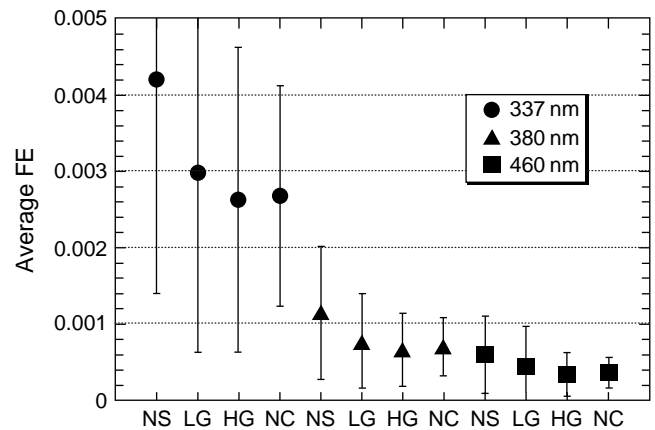

Figure 13 Average fluorescence efficiency (FE) (±standard deviation) for human cervical normal squamous tissues (NS), normal columnar tissues (NC), low-grade SIL (LG) and high-grade SIL (HG) calculated from their fluorescence spectra at the excitation wavelengths 337, 380 and 460 nm. (Reproduced by permission of the Society for Applied Spectroscopy, from McCreery.[70])

5 CLINICAL APPLICATIONS

Currently, one of the most widely explored applications of fluorescence spectroscopy is the detection of endoscopically invisible, early neoplastic growth in epithelial tissue sites. Early neoplastic growth refers to precancerous changes such as dysplasia and carcinoma in situ, which precede invasive cancer or carcinoma. Currently, there are no effective diagnostic techniques for these early tissue transformations. Fluorescence spectroscopy is ideally suited for this application because of its ability to examine tissue surfaces rather than tissue volumes, and its adaptability to an endoscopic device. If fluorescence spectroscopy can be applied successfully as a diagnostic technique in this clinical context, it may increase the potential for curative treatment and thus reduce complications. In addition to the potential for improved patient outcome, the fast and noninvasive nature of this diagnostic technique may also reduce health care costs.

Steady-state fluorescence measurements from small tissue regions (less than a few millimeters in diameter) as well as steady-state fluorescence imaging of relatively large tissue fields (a few centimeters in diameter) have been performed.[11,12] To a much lesser extent, time-resolved fluorescence measurements are being explored currently.[11,12] Furthermore, sources of both intrinsic (endogenous fluorophores) and extrinsic (exogenous fluorophores) fluorescence have been considered.[11,12] The advantage of using exogenous fluorophores is that the photophysical and pharmacokinetic properties can

be selected and are known. Furthermore, exogenous fluorophores are more highly fluorescent than endogenous fluorophores. On the other hand, the disadvantage of using exogenous fluorophores is that issues relating to safety and toxicity of the drug being used have to be addressed. Furthermore, the selection of the optimal time delay after administration of the drug is nontrivial.

Several authors have reviewed the progress in this field over the last decade. Andersson-Engels et al.[5,6] discussed the possibilities of using fluorescence spectroscopy for tissue diagnosis. The tissue types discussed were malignant tumors and atherosclerotic lesions. Studies of endogenous fluorescence as well as exogenous fluorescence with contrast agents were also presented. In a subsequent review, Andersson-Engels et al.[7] reviewed the scientific, technical and practical issues related to the use of fluorescence spectroscopy for tissue diagnosis in clinical oncological applications. Papazoglou[8] presented a review on the diagnosis of malignancies and atherosclerotic plaques using fluorescence spectroscopy. Special emphasis was given to problems that were raised during clinical trials and recent experimental studies, such as the identification of the fluorescent chemical species and the determination of the illumination/collection geometry for fluorescence spectroscopy of tissue. Bigio et al.[9] reviewed fluorescence spectroscopy and elastic scattering spectroscopy of small regions of tissue, whereas Andersson-Engels et al.[10] focused on fluorescence spectroscopy of relatively large tissue fields. Richards-Kortum et al.[11] and Wagnieres et al.[12] have written more comprehensive reviews. The former review focuses on the quantitative aspects of fluorescence spectroscopy. Specifically, this review describes optical interactions pursued for biomedical applications, provides a descriptive framework for light interactions in tissue and, finally, reviews the important endogenous and exogenous molecules and how they are exploited for tissue diagnosis. The latter review, which focuses more on clinical aspects, presents a critical status report on the diagnosis of neoplastic tissues in vivo using fluorescence spectroscopy.

5.1 Neoplasia

5.1.1 Endogenous Fluorescence

The phenomenon of fluorescence was first observed by Stokes.[73] Much later, Stubel recognized the diagnostic potential of tissue fluorescence.[74] Policard[47] observed red fluorescence when examining necrotic tumors under illumination with UV and VIS light. Ronchese[48] demonstrated in 1954 that ulceration is essential for the production of red fluorescence in human cutaneous, squamous cell carcinoma. The observed fluorescence was attributed to endogenous porphyrins in the tissue. Ghadially et al.[39,49−51] also reported that ulcerated

squamous carcinomas exhibit a red fluorescence when exposed to UV light. They concluded that this red fluorescence may be due in part to the action of bacteria on a protoporphyrin precursor. In 1965, Lycette et al.[75] suggested that fluorescence spectroscopy could be used to discriminate between normal tissues and malignant tumors. Fluorescence emission spectra were recorded from excised normal tissue and malignant tumors of the esophagus, stomach, breast and thyroid at 330 nm excitation. All tissues fluoresced in the range 360−600 nm. It was found that the fluorescence intensities of malignant tumors were less than that of normal tissue from the same patient. Subsequently, the groups of Profio,[76,77] Alfano,[78] Lohmann[79] and Yang[80] did pioneering studies on in vitro and in vivo fluorescence spectroscopy of neoplastic and nonneoplastic animal and human tissues.

Fluorescence spectroscopy has been used to evaluate neoplastic and nonneoplastic tissues in vitro and in vivo. Generally, the results of in vitro studies have been used to guide the design of experimental parameters for in vivo studies.[81] However, in vitro studies can introduce significant artifacts due to hemoglobin reabsorption and oxidation of certain fluorophores,[82] questioning the relevance of in vitro studies to in vivo studies. Richards-Kortum et al.[11] review in vitro and in vivo studies on fluorescence spectroscopy of neoplasia and in vitro studies on fluorescence spectroscopy of atherosclerosis. This review covers only in vivo studies, in order to demonstrate the diagnostic potential of fluorescence spectroscopy in clinical applications.

UV/VIS fluorescence spectroscopy can be developed and employed to differentiate diseased from nondiseased tissues in vivo. The altered biochemical and morphological state that occurs as tissue progresses from a nondiseased to a diseased state is reflected in the spectral characteristics of the measured fluorescence. This spectral information can be compared to tissue histology – the current gold standard – which indicates the absence or presence and grade of disease. Mathematical algorithms then can be developed and optimized to classify tissues into their respective histological category based on their spectral features. These mathematical algorithms can be implemented in software, thereby potentially enabling fast, noninvasive, automated screening and diagnosis in a clinical setting. Although the signal-to-noise ratio of fluorescence spectroscopy is several orders of magnitude lower than that associated with absorption spectroscopy over the same wavelength range, this technique affords higher sensitivity and specificity for biochemical characterization.

Table 2[83−100] summarizes the key aspects of a representative set of clinical applications of fluorescence spectroscopy (the most recent investigation per group and investigations from groups who reported the performance

Table 2 Fluorescence spectroscopy of neoplastic and nonneoplastic tissues in vivo obtained from a representative set of clinical applications[a]

Tissue	Excitation wavelength (nm)	Measurement type	Dimension reduction: emission wavelengths (nm)	Classification: decision scheme	Sample size ND; D	SE; SP (%)
Colon[83]	337	Spectra	MVLR (spectra)	Binary	121; 56	80; 92
Colon[84]	337	Spectra	MVLR (spectra)	Binary	182; 32	100; 84
Colon[85]	370	Spectra	I (460, 600, 680)	Bayes theorem	67; 32	94; 91[b]
Colon[86]	360	Images	I (>400)	Binary	12; N/A	83; N/A
Colon[87]	337	Transient decay	τ (550)	Binary	13; 11	85; 87
Cervix[88]	337, 380, 460	Spectra	PCA (spectra)	Bayes theorem	122; 59	82; 68[b]
Cervix[88,89]	337, 380, 460	Spectra	PCA of 15 $I(\lambda_x, \lambda_m)$	Bayes theorem	122; 59	84; 65[b]
			15 $I(\lambda_x, \lambda_m)$	Neural network		91; 67[b]
Bronchus[90]	442	Images	I (red, green)	Binary	558; 142	67; N/A[c]
Bladder[91]	337	Spectra	I (385, 455)	Binary	85; 29	97; 98[d]
Bladder[92]	308	Spectra	I (360, 440)	Binary	35; 31	100; 100[d]
Esophagus[93]	410	Spectra	I (480, 680)	Binary	252; 56	40; 96
Oral cavity[94]	370	Spectra	I (490)	Binary		100; 87.5
	410		I (640)			
Oral cavity[95]	337	Spectra	I (peak)	Binary	17; 11	94; 100
	410		I (635, 490)			
Head and neck[96]	442	Images	I (red, green)	Binary	16; 16	100; 87.5[d]
Head and neck[97]	375–440	Images, spectra	I (>515)	Binary	36; N/A	43.3; N/A[d]
					36; N/A	94.4; N/A[d]
Larynx[98]	442	Images	I (red, green)	Binary	328 total	72.5; 94[c,d]
Larynx[99]	442	Images	I (red, green)	Binary	87; 28	85; 87[c,d]
Skin[100]	336	Images	I (475)	Binary	318; 90[d]	83; 79

[a] Acronyms: I = intensity; τ = decay time; MVLR = multivariate linear regression; PCA = principal component analysis; λ_x = excitation wavelength; λ_m = emission wavelength; ND = nondiseased; D = diseased; SE = sensitivity; SP = specificity; N/A = not applicable.
[b] Sensitivity and specificity were evaluated prospectively.
[c] Sensitivity and specificity were evaluated for a combination of fluorescence and conventional endoscopic techniques.
[d] Sensitivity and specificity were calculated for the discrimination between cancers and noncancers (other investigations calculated the sensitivity and specificity for discriminating precancers and cancers from normal tissues).

of their technique). In these applications, fluorescence spectroscopy in the UV/VIS spectral regions was used for the detection of neoplastic tissues in vivo. In particular, Table 2 provides the organ sites studied, the excitation wavelength(s) used, the type of measurements that were made, the dimensionally reduced spectral variables and the corresponding classification scheme used in the mathematical algorithm, the sample size for the diseased and nondiseased populations and the corresponding sensitivity and specificity. Note that in all these clinical applications only the endogenous fluorescence, absorption and scattering properties of the tissue were exploited.

The neoplastic tissues that were evaluated spectroscopically are from the colon,[83–87] cervix,[88,89] bronchus,[90] bladder,[91,92] brain[101] (preliminary studies only), esophagus,[93] oral cavity,[94,95] head and neck,[96,97] larynx,[98,99] skin,[100] bile duct[102] (preliminary studies only), stomach[103] (in vitro studies only) and breast tissues[104–107] (in vitro studies only). The excitation wavelengths that were selected correspond to those used to excite fluorophores in the UV/VIS spectral regions (see Table 1). Most groups measured fluorescence emission

spectra from tissue sites that are 1–2 mm in diameter. Only a few groups measured fluorescence images from tissue regions that are a few centimeters in diameter, and only one group measured the transient fluorescence decay from colon tissues in vivo.

There are generally two steps involved in the development of a mathematical algorithm that is based on fluorescence spectroscopy. The first part is to reduce dimensionally the measured spectral variables, and the second step is to develop a classification scheme for the discrimination of these useful spectral parameters into relevant histological/histopathological categories. The development of current mathematical algorithms based on fluorescence spectroscopy can be classified broadly into three categories: algorithms based on qualitatively selected spectral variables (fluorescence intensities at several emission wavelengths); algorithms based on statistically selected spectral parameters (a more robust use of all the measured spectral information); and algorithms based on parameters that reflect the biochemical and/or morphological features of the tissue. Classification schemes have been primarily based on a binary discrimination or a probability-based classification scheme.

Mostly, algorithms have been based on qualitatively or statistically selected spectral variables with binary classification schemes as indicated in Table 2.

The sensitivity is defined as the fraction of diseased samples correctly classified, and the specificity is defined as the fraction of nondiseased tissues correctly classified. In several clinical studies, the sensitivity and specificity were evaluated prospectively rather than retrospectively to obtain an unbiased estimate of the performance of this technique.[85,88,89] In some cases the sensitivity and specificity were evaluated for a combination of fluorescence spectroscopy and conventional endoscopy.[90,98,99] Finally, in the case of the bladder, head and neck and larynx, the sensitivity and specificity are reported for the discrimination between cancers and noncancers.[91,92,96–99] In other clinical applications, the sensitivity and specificity are reported for the discrimination of precancers and cancers from normal tissues. In the majority of clinical studies performed the sensitivity and specificity are greater than 80%, reflecting the high classification accuracy of fluorescence spectroscopy for the detection of neoplastic tissues in vivo. The sensitivity and specificity reported here are similar or superior to current clinical modalities that are used routinely.

5.1.2 Exogenous Fluorescence

There are a number of groups that have explored the diagnostic potential of fluorescence spectroscopy of exogenous fluorophores (particularly photosensitizing agents developed for PDT) in tissues in vivo.[12] Auler et al.[108] and Figgie[109] first observed red fluorescence from animal tumors after administration of exogenous porphyrins. The first use of fluorescin to improve the detection and identification of brain tumors in vivo was reported by Moore et al.[110] The accumulation of hematoporphyrin in various types of cancers was discovered and exploited during the 1950s.[111–113] HpDs were evaluated subsequently for localization in cancers of various organs, including the esophagus, tracheobronchial tree and cervix,[114–120] and for characterizing suspicious head and neck lesions.[121] The first cystoscopic observations of HpD fluorescence in urinary bladder tumors were reported by Kelly et al.[122] These and other initial clinical and animal model studies of HpD-mediated PDT led to fluorescence diagnostic applications by many other groups using this exogenous fluorophore. Subsequently, Kreigmair et al.[123] proposed the use of 5-ALA-induced PpIX fluorescence for the detection of bladder neoplasms.

Photosensitizing agents, particularly HpD and 5-ALA, have been used as contrast agents for fluorescence spectroscopy of neoplastic tissues in a wide variety of tissue sites, including the skin, bladder, bronchus, colon, esophagus, head and neck, and breast.[12] However,

because most of these exogenous fluorophores rely on the differences in the vasculature between diseased tissues (which generally exhibit leaky vessels) relative to their nondiseased counterparts, it remains to be seen whether the characteristics that determine localization of the exogenous fluorophore in cancers are also present in precancerous tissues.

5.2 Atherosclerosis

Edholm et al.[124] suggested that quantitative optical techniques could be used to improve the detection of atherosclerosis in vivo; they measured the reflectance of the aorta at 500 and 550 nm in 15 patients undergoing aortography. Kitrell et al.[125] demonstrated that fluorescence spectroscopy could be used to discriminate between normal aorta and fibrous plaque, and suggested that optical diagnosis (using low-power illumination) and therapy (using high-power illumination) of atherosclerosis could be combined in a single fiber-optic device. Subsequently, a number of groups investigated the utility of fluorescence spectroscopy for the diagnosis of atherosclerotic plaque, many with the goal of developing a guidance system for laser angiosurgery catheters.[8,11]

The fluorescence emission spectra of normal artery tissue and atherosclerotic plaques have been measured over the entire range of UV/VIS excitation wavelengths.[11] However, most of these investigational studies to demonstrate the diagnostic potential of fluorescence spectroscopy have been performed in vitro on excised tissues and hence have not addressed the problems of making these measurements in vivo on the intact artery wall.

6 CLINICAL INSTRUMENTS

In this section representative examples of instruments used in clinical applications of fluorescence spectroscopy are described. In particular, details of the instruments and typical data are presented to provide the reader with an understanding of the main characteristics of instruments for UV/VIS fluorescence spectroscopy.

6.1 Single-pixel, Three-excitation-wavelength Fluorimeter

Although fluorescence emission spectra of normal tissue, dysplasia and invasive carcinoma have been measured previously from several organ sites in vivo at single excitation wavelengths (see Table 2), Ramanujam et al.[88] were among the first to address the necessity to measure fluorescence emission spectra at several excitation

wavelengths in order to exploit more fully the tissue biochemistry and morphology. They developed a portable fluorimeter that can be used to measure fluorescence emission spectra from 1-mm-diameter human cervical tissue sites in vivo at three excitation wavelengths in the UV/VIS spectral regions. These wavelengths were selected primarily because they coincide with the absorption bands of biologically relevant fluorophores, namely the metabolic coenzymes and structural proteins and chromophores, which include oxygenated and deoxygenated hemoglobin. A schematic of the fluorimeter is shown in Figure 14.

Two nitrogen pumped-dye lasers (5 ns pulse duration, 30 Hz repetition rate) are used to provide illumination at three different excitation wavelengths: one laser generates light at 337 nm (fundamental) and has a dye module in a resonant cavity that can be used to generate light at 380 nm using the fluorescent dye BBQ. The dye module in the resonant cavity of the second laser is used to generate light at 460 nm, using the fluorescent dye Coumarin 460. Laser illumination at each excitation wavelength of 337, 380 and 460 nm is coupled to each of three excitation fibers in a fiber-optic probe. Note that two 10-nm bandpass filters – one centered at 380 nm and the other centered at 460 nm – are placed between the excitation fiber and the two dye modules, to prevent leakage from the fundamental at 337 nm.

The fiber-optic probe consists of a central fiber surrounded by a circular array of six fibers; all seven fibers have the same characteristics (0.22 numerical aperture, 200 μm core diameter, 245 μm diameter with cladding). Three fibers along the diameter of the distal end of the probe are used for excitation light delivery. The purpose of the remaining four fibers is to collect the emitted light from the tissue area directly illuminated by the excitation light.[57,58] A quartz shield (3 mm in diameter and 2 mm thick) at the tip of the distal end of the probe, which is in direct tissue contact, provides a fixed distance between the fibers and the tissue surface so that the fluorescence intensities can be measured in calibrated units. A tissue area that is 1 mm in diameter is illuminated by each excitation delivery fiber. The average energies per pulse on the tissue surface at 337, 380 and 460 nm excitation were 15.2, 11.5 and 18 $\mu J\,mm^{-2}$, respectively, in this case.

The proximal ends of the four emission collection fibers are arranged in a circular array and imaged at the 500-μm-wide entrance slit of an f 3.8 spectrograph equipped with a 300 grooves mm^{-1} grating coupled to a 1024-intensified PDA controlled by a multichannel analyzer. The collection optics between the proximal end of the four fibers and the spectrograph are two, fused-silica, planoconvex lenses. Between these lenses is a filter wheel assembly containing long-pass filters with 50% transmission at 360, 400 and 475 nm, which are used to reject backscattered excitation light at 337, 380 and 460 nm excitation, respectively, from the detector. The nitrogen pumped-dye lasers are used for external triggering of a pulser, which serves to synchronize the 200-ns collection gate of the detector to the leading edge of the laser pulse. The use of gated detection in conjunction with pulsed excitation eliminates the effects of ambient light during fluorescence measurements. The total time required to record fluorescence emission spectra at all three excitation wavelengths from one tissue site was approximately 5 s. Spectra were collected in the VIS spectral region, with a resolution of 10 nm (fwhm)
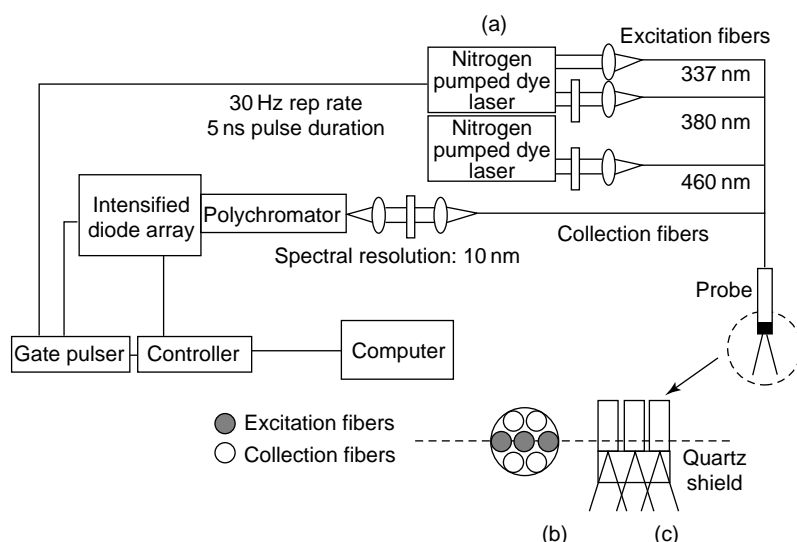

Figure 14 Schematic of a three-excitation-wavelength system. (Reproduced by permission of the American Society for Photobiology, from Ramanujam et al.[88])

and a signal-to-noise ratio of 100 : 1 at the fluorescence maximum at each excitation wavelength. Data acquisition and storage are achieved using a computer.

All spectra were corrected for the nonuniform spectral response of the detection system using correction factors obtained by recording the spectrum of a National Institute of Standards and Technology (NIST) traceable, calibrated, tungsten ribbon filament lamp. Spectra from each cervical tissue site at each excitation wavelength were averaged to obtain a single spectrum per site. The average tissue spectra were then normalized to the average peak fluorescence intensity of the rhodamine 610 calibration standard at the corresponding excitation wavelength for that patient; absolute fluorescence intensities are reported in these calibrated units.

Figure 15 illustrates average fluorescence emission spectra per site acquired from cervical tissue sites at 337, 380 and 460 nm excitation from a typical patient. All fluorescence intensities are reported in the same set of calibrated units. Evaluation of the tissue spectra at 337 nm excitation indicates that the fluorescence

Figure 15 Fluorescence spectra measured at 337, 380 and 460 nm excitation from the cervix of a typical patient using the three-excitation-wavelength fluorimeter. (Reproduced by permission of the American Society for Photobiology, from Ramanujam et al.[88])

intensity of the precancerous SIL is less than that of the corresponding normal squamous tissue and greater than that of the corresponding normal columnar tissue. Evaluation of the spectra at 380 nm excitation indicates that the fluorescence intensity of SIL is less than that of the corresponding normal squamous tissue, with the low-grade SIL exhibiting the weakest fluorescence intensity. Note that the fluorescence intensity of the normal columnar tissue is indistinguishable from that of the high-grade SIL. Finally, evaluation of spectra at 460 nm excitation indicates that the fluorescence intensity of SIL is less than that of the corresponding normal squamous tissue and greater than that of the corresponding normal columnar tissue. The spectra shown here demonstrate that it is possible to obtain fluorescence emission spectra from tissues in vivo at several excitation wavelengths, with a high signal-to-noise ratio and in a fast and noninvasive manner.

6.2 Single-pixel, Excitation–Emission Matrix System

It is apparent that fluorescence emission spectra at multiple excitation wavelengths spanning the UV/VIS spectral regions are needed to characterize properly the patho-physiologically relevant, endogenous fluorophores in tissue. Furthermore, reflectance measurements at these wavelengths are also needed to probe tissue absorption and scattering properties and enable deconvolution between the fluorescence, absorption and scattering.[126,127] Zeng et al.[128] developed an instrument to measure the fluorescence emission spectra and diffuse reflectance spectra from the human skin, simultaneously. However, this instrument was capable of measuring fluorescence emission spectra at only a single excitation wavelength of 380 nm.

Zangaro et al.[69] integrated and improved upon the designs of Ramanujam et al.[88] and Zeng et al.[128] by constructing a fast EEM system that can measure fluorescence emission spectra at multiple excitation wavelengths and diffuse reflectance spectra from 1- to 2-mm-diameter tissue sites in vivo quickly and noninvasively. Preliminary considerations for the design of this system were as follows: rapid wavelength tunability and real-time data acquisition for fluorescence spectroscopy at multiple excitation wavelengths; the ability to measure diffuse reflectance in addition to fluorescence; gated detection of spectral measurement with minimal interference from ambient light; and capability for optical fiber delivery and collection. The system, which was designed with the aforementioned considerations in mind, is shown in Figure 16.

A nitrogen pumped-dye laser is used as the excitation light source. Delivery of light to tissue and collection of returned spectral information is accomplished by
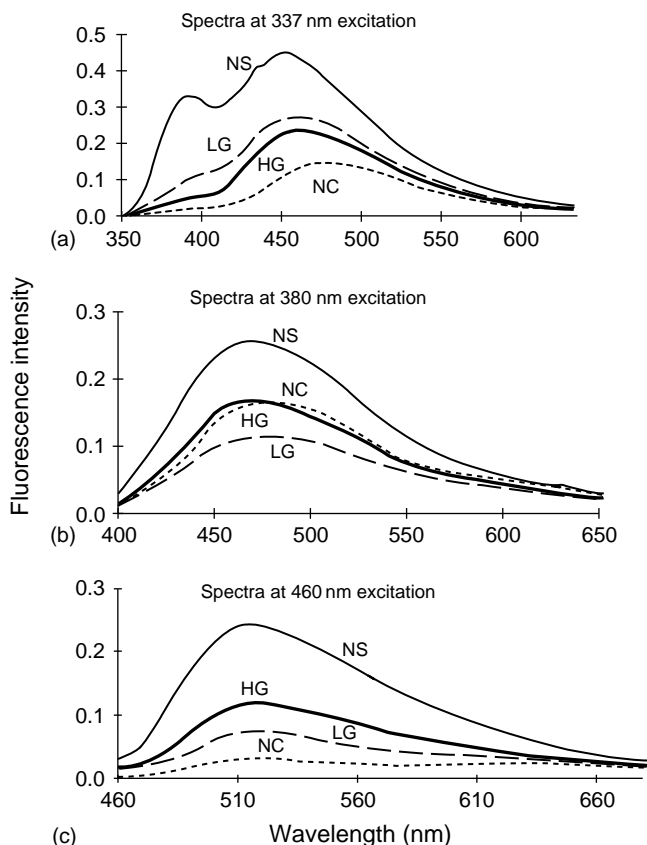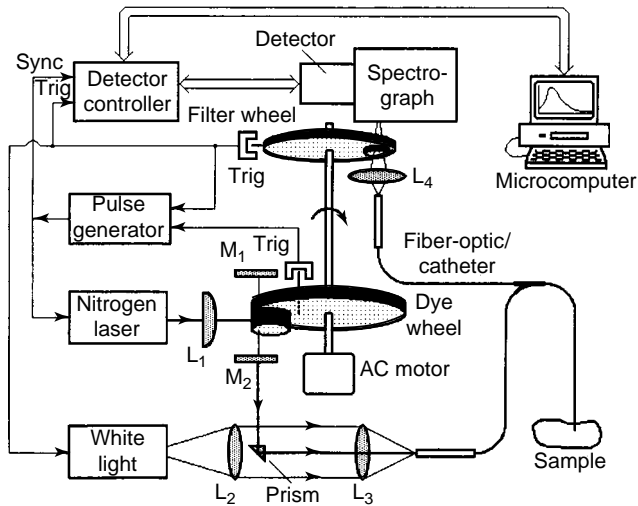
Figure 16 EEM system designed to measure tissue fluorescence spectra at multiple excitation wavelengths and spectrally resolved broad band diffuse reflectance spectra in vivo. (Reproduced by permission of the Optical Society of America, from Zangaro et al.[69])

means of an optical fiber probe. A filter wheel placed in front of the spectrograph rejects backscattered excitation light. The fluorescence is dispersed in the spectrograph, detected by an intensified PDA, coupled to an optical multichannel analyzer and stored in a computer. The novel aspects of this system, which lends itself to multi-excitation fluorescence spectroscopy and diffuse reflectance spectroscopy of tissues in the UV/VIS spectral regions, are described below.

Dye cuvettes (with appropriate dyes) mounted on a rotating wheel that rapidly traverses a single resonant cavity are capable of generating multiple wavelengths. Also, a corresponding filter wheel placed in front of the spectrograph allows rejection of backscattered excitation light at each wavelength when synchronized with the dye wheel. Furthermore, a 10-μs pulsed xenon lamp is also incorporated such that diffuse reflectance measurements can be made over the UV/VIS spectral regions. Fiber-optic delivery and collection have been designed to provide for the remote operation of the system and for the measurement of fluorescence and diffuse reflectance directly from the tissue area that is illuminated, in order to remove the effects of the illumination/collection geometry.[57,58] Furthermore, the fiber-optic probe was designed such that the diffuse reflectance and fluorescence can be made from the same tissue site. The acquisition time for both fluorescence and reflectance measurements is less than 1 s.

The performance of this system has been validated clinically by passing the fiber-optic probe through one of the accessory channels of a colonoscope and bringing
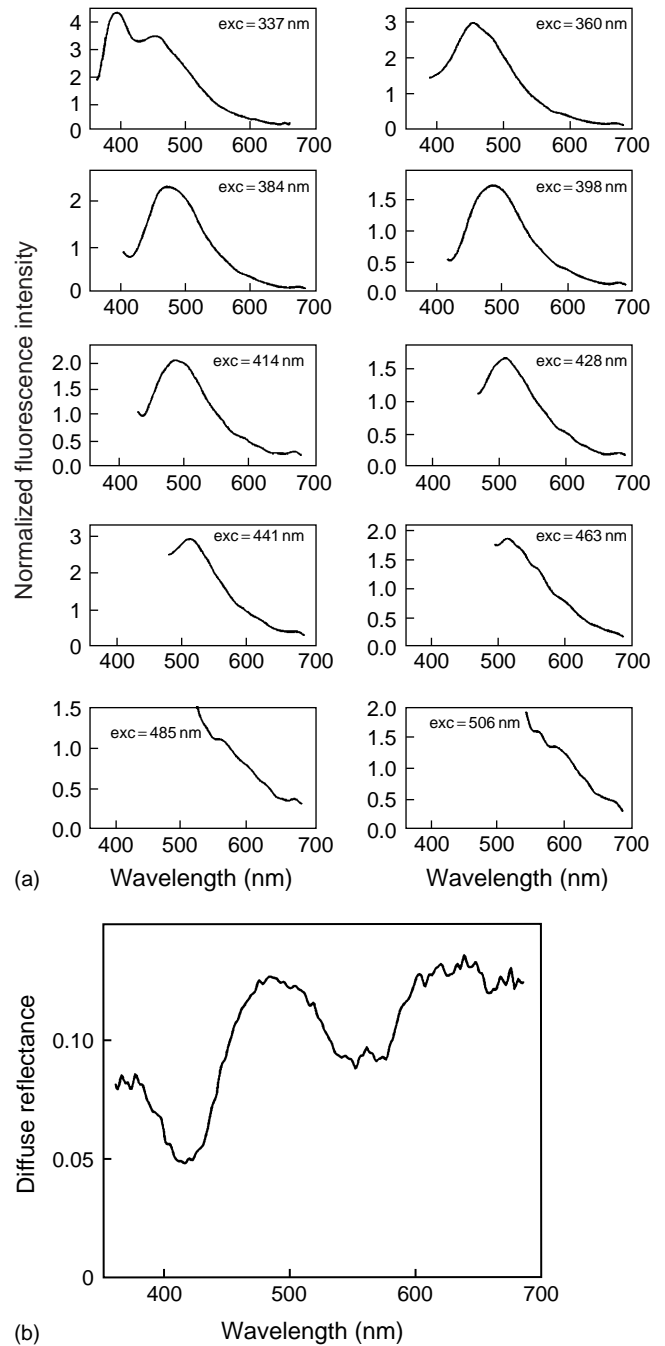
Figure 17 (a) Fluorescence spectra at 10 excitation wavelengths and (b) diffuse reflectance spectrum over the UV/VIS spectral regions measured from a colon tissue site in vivo. (Reproduced by permission of the Optical Society of America, from Zangaro et al.[69])

it into flush contact with the tissue surface. Figure 17(a) displays fluorescence emission spectra at multiple excitation wavelengths and Figure 17(b) displays a diffuse reflectance spectrum from colon tissue. Figure 17(a) shows spectra measured at 10 excitation wavelengths in

the UV/VIS spectral regions. The spectra at the different excitation wavelengths appear to correspond with spectra of biologically relevant fluorophores, including collagen (337 nm excitation), reduced PN (360 nm excitation) and oxidized Fp (428 nm excitation). Note that the effects of hemoglobin absorption on the fluorescence emission spectra are observed at 337 nm excitation. Figure 17(b) shows the diffuse reflectance spectrum obtained from the same tissue site. The spectrum exhibits the absorption bands of hemoglobin at 420 nm (Soret band) and at 540 and 580 nm (α and β bands).

Zuluaga et al.[129] have also developed a fast EEM system that measures fluorescence emission spectra at multiple excitation wavelengths and diffuse reflectance spectra rapidly (4 min total measurement time) and non-invasively from tissues in vivo. Specifically, the system measures the fluorescence EEM at 330–500 nm excitation and 380–700 nm emission. The diffuse reflectance spectra are measured at 380–950 nm. The primary difference between this system and that developed by Zangaro et al.[69] is that it employs a white light source with a series of bandpass filters instead of a nitrogen pumped-dye laser for generating multiple excitation wavelengths for fluorescence spectroscopy. Furthermore, Zuluaga et al.[129] present a method based on autocorrelation vectors to identify the excitation and emission wavelengths where the spectra of diseased and nondiseased tissues differ the most.

6.3 Fluorescence Imaging Systems

Several groups have developed endoscopic-compatible[86,97,130–134] and nonendoscopic-based[100,135,136] fluorescence imaging systems. The most notable is that originally developed by Palcic et al. for fluorescence bronchoscopy,[130] which has now led to a commercial light-induced fluorescence endoscopy (LIFE) device (Xillix Technologies Corporation, Richmond, BC, Canada) that is used for fluorescence imaging of relatively large tissue fields (a few centimeters in diameter). The LIFE device consists of a white light source and a color CCD for the acquisition of white light images, a helium–cadmium laser and two filtered, high-sensitivity CCD cameras for the acquisition of green and red fluorescence images, an endoscope-compatible fiber-optic bundle and a computer with a monitor. The laser is used to provide excitation light at 442 nm. The fluorescence emitted is collected and coupled via an imaging, fiber-optic bundle to two filtered, image-intensified CCD cameras (one for the green wavelength band at 480–520 nm and one for the red wavelength band at 630 nm and longer). The fluorescence image is digitized using an imaging board in the computer. Using a mathematical transformation (a nonlinear discriminant function combination of the red and green

intensity images), a pseudo-image of the observed tissue site is obtained and displayed on the monitor in real-time. Normal tissues appear green and neoplastic tissues appear brownish-red.

The LIFE device has been tested in a multicenter clinical trial to evaluate if fluorescence bronchoscopy, when used as an adjunct to white light bronchoscopy, can improve the bronchoscopist's ability to locate areas suspicious of dysplasia for biopsy and histological examination as compared to white light bronchoscopy alone.[90] The LIFE device also has been used successfully to evaluate neoplastic lesions in other organ sites, including the head and neck,[96] larynx,[98,99] bile duct,[102] and gastrointestinal tract.[137,138]

Recently, Zeng et al.[134] elaborated on the fluorescence imaging system for the gastrointestinal tract. The device consists of a mercury arc lamp, two intensified CCD cameras, a fiber-optic endoscope and a computer-based console. The system is capable of working in three different modalities: conventional white light imaging mode; light-induced fluorescence imaging mode, based on fluorescence imaging of two wavelength bands in the red and green; and light-induced fluorescence and reflectance imaging mode, based on the combination of red and green fluorescence images and a red-NIR reflectance image.

7 METHODS OF ANALYSIS

Most screening and diagnostic algorithms developed from fluorescence spectroscopy of tissues incorporate qualitatively or statistically selected spectral variables, which are evaluated using a binary or probability-based classification scheme. For example, Panjehpour et al.[93] have developed an algorithm that uses qualitatively selected, fluorescence intensities at several emission wavelengths in a binary classification scheme for the detection of Barrett's esophagus in vivo. On the other hand, Ramanujam et al.[88] have developed an algorithm that uses statistically selected spectral variables and probability-based classification for cervical precancer detection in vivo. This multivariate statistical algorithm employs PCA[139] to reduce dimensionally the preprocessed tissue fluorescence emission spectra into orthogonal principal components with minimal information loss. Bayes theorem[140] is then used to develop probability-based classification using the diagnostically relevant principal components. The advantage of using statistical rather than qualitative analysis of the tissue fluorescence emission spectra is that the entire spectral information content can be exploited. Furthermore, the benefit of using a probability, rather than a binary, classification scheme is that the likelihood of the classification being correct is also provided.

An example of an algorithm that uses biochemical and/or morphological features that are related to the tissue fluorescence emission spectra, coupled with a probability-based classification, is that developed by Richards-Kortum et al.[141] This algorithm discriminates between normal coronary arteries and noncalcified and calcified atherosclerotic plaque in vitro. The contribution of the biochemical and/or morphological features is extracted from the tissue fluorescence emission spectra via an analytical model of tissue fluorescence, based on the exponential attenuation of light in an absorption-dominant medium. Bayes' theorem is then used for probability classification.

The advantage of using a physically based model over a statistically based model is that the former method provides insight into the biochemical and morphological basis. However, there are notable advantages to using a statistical model such as PCA. Although it is a linear method of analysis, PCA can still be used to model effectively the nonlinear turbid tissue fluorescence. Because it is less restrictive, PCA can permit a better fit to the fluorescence emission spectra than simple physical models can, through the use of a linear combination of orthogonal principal components.[142] In addition, the principal components are not correlated with each other and therefore can be used in a variety of classification algorithms that generally require un-correlated variables. Furthermore, each principal component can be correlated to the spectral variables of the original tissue fluorescence emission spectra, thus providing insight into the spectral features that contribute to the classification.

Most algorithms to date use qualitatively and, to a lesser extent, statistically selected variables with binary or probability-based classification schemes as indicated in Table 2. The development of a physically based model that uses biochemical and morphological features that are related to the measured tissue fluorescence emission spectra has been hampered by the fact that fluorescence spectroscopy of human tissue is greatly affected by the absorption and scattering of the excitation light and the emitted light, making interpretation of the measured spectral information challenging.[53]

Given the high classification accuracy that can be achieved using statistically based algorithms,[88] and the difficulties associated with the development of physically based algorithms,[141] it is perhaps worthwhile considering the development of a hybrid algorithm that incorporates the key features of both. For example, the statistical model could be related to the physical model in order to realize the biochemical and/or morphological basis of the statistically selected spectral variables that are used for classification purposes.

Section 7.1 provides a detailed description of the algorithm developed by Ramanujam et al.,[88] which uses statistically selected spectral parameters in conjunction with a probability based classification process. Section 7.2 discusses physically based models to analyze tissue fluorescence emission spectra and their potential to elucidate the biochemical and morphological features that contribute to the tissue fluorescence emission spectra. Section 7.3 presents various approaches to account for the illumination/collection geometry-related distortion of the tissue fluorescence emission spectra measured in vivo.

7.1 Statistically Based Model

Ramanujam et al.[88] developed a formal analytical process for the development of screening and diagnostic algorithms for the detection of human cervical precancer or SIL in vivo. The formal analytical process is displayed in Figure 18, where the text in the dashed-line boxes represents the mathematical steps implemented on the spectral data, and the text in the solid-line boxes represents the output after each mathematical process. There are four primary steps involved in the multivariate statistical analysis of tissue fluorescence emission spectra. The first step is to preprocess spectral data to reduce interpatient and intrapatient variation within a tissue type; the preprocessed spectra are then dimensionally reduced to an informative set of principal components that describe most of the variance of the original spectral data set using PCA.[139] Next, the principal components that contain diagnostically relevant information are selected using an unpaired, one-sided Student's t-test, and finally a classification algorithm based on Bayes theorem[140] is developed using these diagnostically relevant principal components.

In summary, three constituent algorithms were developed using multivariate statistical analysis: constituent algorithm 1 discriminates between SIL and normal squamous tissues; constituent algorithm 2 discriminates between SIL and normal columnar tissues; and algorithm 3 differentiates high-grade SIL from low-grade SIL. The three constituent algorithms were then combined to develop two composite algorithms: constituent algorithms 1 and 2 were combined to develop a composite screening algorithm that discriminates between SIL and non-SIL. All three constituent algorithms were then combined to develop a composite diagnostic algorithm that differentiates high-grade SIL from non-high grade SIL.

Inputs into the multivariate statistical algorithm included the preprocessed fluorescence spectra at all three excitation wavelengths (full-parameter) and fluorescence intensities at a reduced number of excitation–emission wavelength pairs (15 reduced parameters) selected from the component loadings calculated from PCA.[139] The
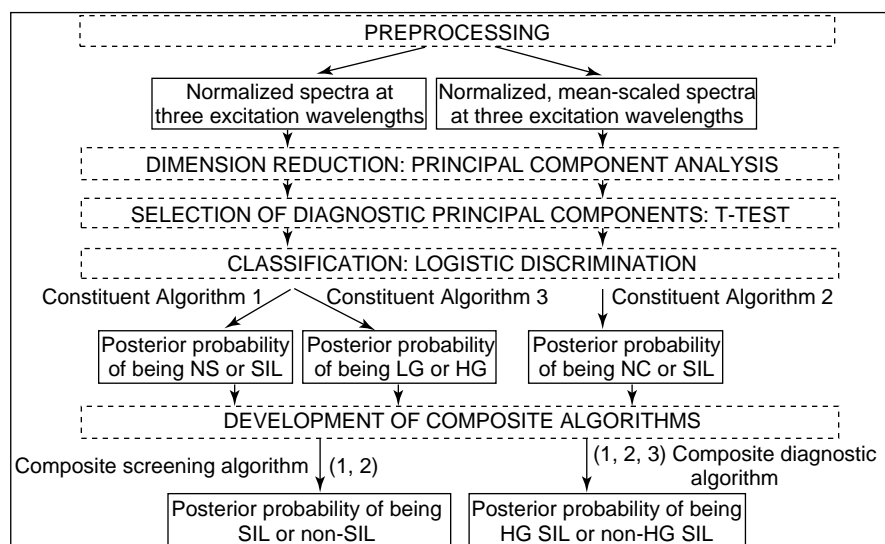
Figure 18 Formal analytical process for the development of screening and diagnostic algorithms for the differential detection of cervical pre-cancer or SILs. NS = normal squamous; NC = normal columnar; LG = low grade; HG = high grade. (Reproduced by permission of the American Society for Photobiology, from Ramanujam et al.[88])

Table 3 Comparison of accuracy of composite screening and diagnostic (full and reduced-parameter) algorithms to that of Pap smear screening and colposcopy in expert hands

Classification	SIL $v.$ Non-SIL		HG SIL $v.$ Non-HG SIL	
	Sensitivity (%)	Specificity (%)	Sensitivity (%)	Specificity (%)
Pap smear screening	62 ± 23	68 ± 21	N/A	N/A
Colposcopy in expert hands	94 ± 6	48 ± 23	79 ± 23	76 ± 13
Full-parameter composite algorithm	82 ± 1.4	68 ± 0.0	79 ± 2	78 ± 6
Reduced-parameter composite algorithm	84 ± 1.5	65 ± 2	78 ± 0.7	74 ± 2

HG = high grade; N/A = not applicable.

algorithm was developed on a calibration set and tested on a prediction set of approximately equal numbers of samples in each tissue category.

Table 3 compares the sensitivity and specificity of the composite screening and diagnostic algorithms with that of Pap smear screening[143] and colposcopy in expert hands.[144] Table 3 indicates that the composite screening algorithm has a similar specificity and a significantly improved sensitivity relative to Pap smear screening. A comparison of the composite screening algorithm to that of colposcopy in expert hands for differentiating SIL from non-SIL indicates that this algorithm demonstrates a 10% decrease in sensitivity but a 20% improvement in specificity. The composite diagnostic algorithm and colposcopy in expert hands both discriminate high-grade SIL from non-high-grade SIL with a similar sensitivity and specificity. Finally, the sensitivity and specificity of the reduced-parameter algorithms that use an order of magnitude fewer variables is within 5% of the sensitivity and specificity reported for the full-parameter

algorithms. This has important implications in using fluorescence spectroscopy to identify fluorescence intensities at a reduced number of optimal excitation–emission wavelength pairs for the implementation of fluorescence imaging.

7.2 Physically Based Models

Although it has been demonstrated that fluorescence spectroscopy can be used to differentiate diseased from nondiseased tissues with high sensitivity and specificity, the underlying biochemical and morphological basis for the spectral differences is poorly understood. This has been hampered by the fact that fluorescence spectroscopy of a turbid medium such as tissue is complicated by its absorption and scattering properties.[53]

A fluorescence emission spectrum measured from tissue over the UV/VIS spectral region is primarily attributed to the superposition of the fluorescence of a variety of biological molecules that contain naturally occurring fluorophores. Fluorescence emission spectra

measured from tissues also contain information about the absorbing and scattering properties of that medium. Quantification of the concentration and distribution of fluorophores within tissue in principle involves: deconvoluting the absorption and scattering properties of the tissue from the measured fluorescence emission spectrum; and quantifying the identity and distribution of the fluorophores that contribute to the deconvolved spectrum. The former step requires the development of a transfer function based on the measurements of tissue optical properties, whereas the latter step requires knowledge of the identity and distribution of the fluorophores within the tissue.

7.2.1 Transfer Function

Deconvolution of the absorption and scattering properties of the tissue from the measured fluorescence emission spectrum requires knowledge of the tissue optical properties, i.e. the absorption coefficient, the scattering coefficient and the anisotropy parameter. Analytical methods based on Kubelka–Munk theory[61] and the adding–doubling method[62] have been developed to calculate tissue optical properties in the UV/VIS spectral range. However, these models require the measurement of diffuse transmittance and reflectance from tissues. Diffuse transmittance measurements cannot be made from tissues in vivo, thus limiting the number of parameters needed to determine tissue optical properties using these simple analytical techniques.

Several groups have developed simple analytical models based on measurements of fluorescence and diffuse reflectance only (no transmittance measurements are needed) to deconvolve absorption and scattering properties of the tissue from the measured fluorescence emission spectrum.[126,127] These analytical techniques, although simplistic, do provide a first step towards quantifying the biochemical and morphological characteristics of tissue fluorescence emission spectra.

In particular, Gardner et al.[127] have developed an analytical expression for recovering the intrinsic fluorescence coefficient (which is defined as the product of the fluorophore absorption coefficient and the fluorescence quantum yield) of a homogeneous turbid medium from a surface measurement of fluorescence and diffuse reflectance. The intrinsic fluorescence coefficient $\beta(\lambda_x, \lambda_m)$ is defined simply by Equation (10):

$$\beta(\lambda_x, \lambda_m) = \mu_a(\lambda_x)\phi(\lambda_m) \qquad (10)$$

where λ_x is the excitation wavelength, λ_m is the emission wavelength, $\mu_a(\lambda_x)$ is the absorption coefficient of the fluorophore at the excitation wavelength and $\phi(\lambda_m)$ is its fluorescence quantum yield at the emission wavelength.

Using the analytical method developed by Gardner et al., one can recover the intrinsic fluorescence coefficient from the measured fluorescence using Equation (11):

$$\beta(\lambda_x, \lambda_m) = \frac{F(\lambda_x, \lambda_m)}{P_0(\lambda_x)[(\Delta\Omega/\pi)\cos\theta]D(\lambda_m)X_{1D}(\lambda_x, \lambda_m)}$$
$$(11)$$

where $F(\lambda_x, \lambda_m)$ is the measured fluorescence intensity, $P_0(\lambda_x)$ is the power of the incident light at the excitation wavelength, D is the detector's wavelength-dependent response function, $[(\Delta\Omega/\pi)\cos\theta]$ is the detector collection efficiency for a distant detector geometry and a tissue surface with Lambertian intensity distribution, and X_{1D} is the one-dimensional path length factor. The term $P_0(\lambda_x)[(\Delta\Omega/\pi)\cos\theta]D(\lambda_m)$ can be quantified by calibration of the fluorescence measurement for source and detector constants. Specifically, the fluorescence calibration can be performed with an optically dilute fluorophore solution with a predetermined intrinsic fluorescence coefficient. The path length factor X_{1D} requires knowledge of the tissue optical properties at the excitation and emission wavelengths. This function is based upon the exponential attenuation of light away from the source, as are the Beer–Lambert and diffusion theories, with coefficients that are empirically developed from extensive Monte-Carlo simulations. Factor X_{1D} can be calculated from noninvasive measurements of the diffuse reflectance (R_d) and effective penetration depth (δ). Because two optical properties are needed, it is possible to make two, unique, diffuse reflectance measurements with two illumination–collection fiber distances in order to specify R_d and δ.

The recovery method presented successfully identifies the intrinsic fluorescence coefficient (both spectral line shape and intensity) of turbid tissue phantoms that incorporate various concentrations of fluorophore (rhodamine 6G), absorber (adult hemoglobin) and scatterer (polystyrene spheres) with absorption and scattering coefficients that coincide with the range found in soft tissues. The results are shown in Figure 19. Furthermore, fluorophore concentrations of the turbid tissue phantoms are predicted to within 15% of the true concentration (not shown).

Although this analytical model is simple and can recover the intrinsic fluorescence coefficient from turbid tissue phantom fluorescence emission spectra, there are several limitations associated with it. The optical properties of the medium need to be uniform. Furthermore, the size of the medium should be large enough such that only the surface boundary affects the distribution of light. Finally, the one-dimensional fluence rate expression is valid for collimated incident light with a beam diameter that is at least a factor of four larger than the penetration depth of the light.
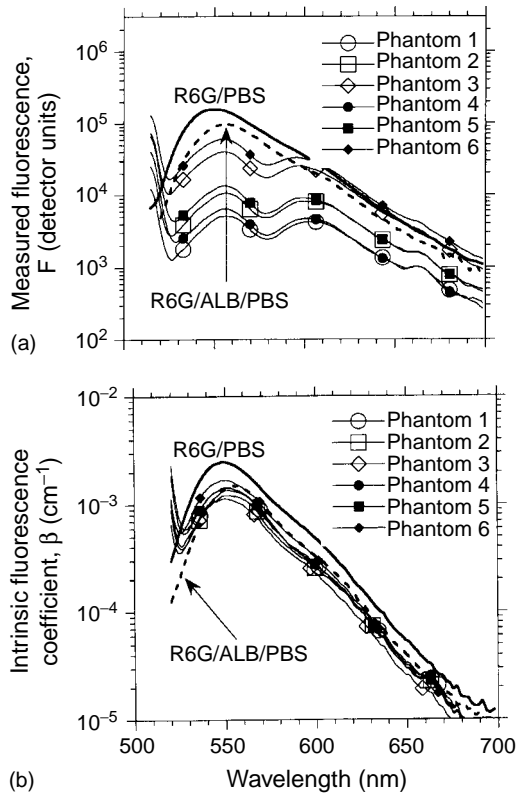
Figure 19 Summary of intrinsic fluorescence recovery from six turbid tissue phantoms: (a) measured uncorrected fluorescence spectra; (b) corrected fluorescence spectra, displayed as the intrinsic fluorescence coefficient β. Note that R6G/PBS corresponds to the fluorescence of rhodamine 6G in phosphate-buffered saline and that R6G/ALB/PBS corresponds to the fluorescence of rhodamine 6G in 2.5% bovine serum albumin–phosphate-buffered saline. (Reproduced by permission of the Optical Society of America, from Gardner et al.[127])

Wu et al.[126] have achieved a similar goal as Gardner et al.[127] using a photon migration approach to model fluorescence from a homogeneous turbid medium such as tissue. The model provides an analytical relationship between the bulk fluorescence emission spectrum F and the diffuse reflectance spectrum R for arbitrary geometries and boundary conditions, which represents an advantage over the previous analytical model.[126] Wu et al. demonstrate that the distortion can be removed by measuring R from a turbid medium over the same wavelength range and with the same geometry as is used for measuring F. The validity of this approach has been demonstrated from tissue experiments using human aortic media and with Monte-Carlo simulations. This analytical model does provide accurate fluorescence line shape information, but unlike the previous analytical model[126] the absolute intensity is still coupled to the absorption coefficient. This implies that the fluorescence measurements from two tissues that have the

same amount of fluorophore but different amounts of absorption will have the same line shape but different fluorescence intensities.

Unlike Gardner et al.[127] and Wu et al.,[126] Panou-Diamandi et al.[145] modeled tissue fluorescence using electromagnetic theory. In this mathematical approach, the inelastic property of fluorescence was expressed via the polarization vector of the medium. The fluorescence scattering spectral function was independent of the excitation and emission geometry, expressing the energy transfer from the excitation frequency to all the emission frequencies. The model assumed that the tissue is a single, homogeneous, infinitely thick dielectric layer under plane wave illumination. Experimental measurements were carried out on optically turbid collagen gels that contained fluorescent dyes, in order to validate the mathematical model. Comparison between experimental and theoretically expected fluorescence emission spectra gave satisfactory results.

Another technique that has been employed to deconvolve the absorption and scattering properties from the fluorescence emission spectra of turbid media is partial least squares (PLS) regression.[146] This method is not based on analytical approximations of the transport equations[126,127] or Maxwell's equations,[145] but rather describes the fluorescence emission spectra measured from turbid medium as a linear combination of basis vectors that are representative of those to be predicted. The PLS method involves the regression between a fluorescence spectral matrix $X(n \times m)$ and a concentration matrix $Y(n \times p)$. PLS seeks a calibration matrix $B(m \times p)$ such that Equation (12) holds:

$$Y = XB \tag{12}$$

The PLS method was compared to models of light transport based on Beer's law[147] and Kubelka–Munk theory[56] to determine which is most effective in extracting the concentration of fluorophores in a set of turbid tissue phantoms containing absorbers and scatterers. The model based on Beer's law significantly underestimated the fluorophore concentrations, whereas the model based on Kubelka–Munk theory significantly overestimated the concentrations. However, this method overestimated the concentrations by a constant scaling factor that potentially can be corrected for. Finally, using the PLS method, which was trained on a set of turbid tissue phantom spectra that have optical properties similar to those to be analyzed, fluorophore concentrations were predicted to within 5% of the true concentration. It should be noted that the success of the PLS method relies on a training set that reflects the chemical and optical

complexity of the turbid media to be investigated. Several important obstacles remain before PLS can be applied to analyze fluorescence emission spectra from tissues. The main obstacle is the question of how to construct reliably a training set in which the concentrations of fluorophores and absorbers of biological interest can be quantified.

7.2.2 Identity and Distribution of Fluorophores that Contribute to Tissue Fluorescence Emission Spectra

It was mentioned earlier that quantification of the concentration of fluorophores within tissue in principle involves two steps. The first step requires deconvolution of the absorption and scattering properties of the tissue from the bulk tissue fluorescence emission spectrum. The second step requires knowledge of the identity and distribution of the fluorophores within the tissue. Although the previously described analytical models[126,127,145,146] address the first step, they do not address the second. The following example addresses the second step specifically through the measurement and quantification of the biochemical and morphological basis of colonic tissue fluorescence emission spectra measured in vivo.[52]

Zonios et al.[52] measured and quantified the contribution of the fluorescent microstructures in frozen, unstained tissue sections to the tissue fluorescence emission spectra measured from colonic tissues in vivo. In order to achieve this, first fluorescence emission spectra were measured at 370 nm excitation from normal colon tissues and colonic adenomas (precancer) in vivo. Deconvolution of absorption and scattering from fluorescence emission spectra measured from the tissues in vivo was achieved using optical properties obtained from Kubelka–Munk[61] analysis of diffuse transmittance and reflectance measurements of excised human colon tissues in vitro. Fluorescence, microscopy and microspectrofluorimetry at 363 nm excitation of thin, frozen, unstained tissue sections were used to characterize the spectral line shapes and the distribution of the fluorescent microstructures that contribute to the measured fluorescence emission spectra of colonic tissues in vivo. A model based on Monte-Carlo simulations[65] was used to relate the spectral line shape and distribution of the fluorescent microstructures to the colonic tissue spectra measured in vivo. This is perhaps one of the first comprehensive attempts to measure and quantify the biochemical and morphological basis of tissue fluorescence emission spectra measured in vivo.

The model developed by Zonios et al.[52] describes the tissue fluorescence emission spectrum $F(\lambda_x, \lambda_m)$, as shown by Equation (13):

$$F(\lambda_x, \lambda_m) = \kappa \sum_i \int \phi_i(\lambda_m) D_i(z) T(\lambda_x, \lambda_m, z) \, dz \quad (13)$$

where λ_x represents the excitation wavelength, λ_m represents the emission wavelength, z represents the depth within the tissue sample, ϕ_i represents the intrinsic fluorescence of each individual microstructure with index i, $D_i(z)$ represents the fluorescence intensity spatial distribution of an individual microstructure with index i, $T(\lambda_x, \lambda_m, z)$ is a transfer function that incorporates the tissue optical properties and is calculated using Monte-Carlo simulations of light propagation in tissue, and κ represents a scaling factor.

First, a database of fluorescence line shapes and distributions of fluorescent microstructures within colon tissue were obtained. A microspectrofluorimeter incorporating a fluorescence microscope, an argon laser source (363.8 nm), a spectrograph and an intensified PDA, coupled to an optical multichannel analyzer was used to record the fluorescence emission spectra of microstructures from unstained, frozen tissue sections cut from tissue biopsies. Quantitative fluorescence imaging studies to quantify the distribution of the fluorescent microstructures within the tissue section were performed using a 75-W short-arc filtered xenon lamp (380 nm) coupled to a microscope and a thermoelectrically cooled CCD camera.

Finally, the transmission and reflection spectra of thick samples of normal mucosa and adenomatous polyps were measured in the range 300–700 nm using a spectrophotometer equipped with an integrating sphere. The tissue absorption and scattering properties were determined by calculating the Kubelka–Munk coefficients[61] and transforming these into transport theory absorption and reduced scattering coefficients.[148] The anisotropy parameter was obtained from the literature for tissues with histology similar to the colon.[53] The transfer function was determined using Monte-Carlo simulations.[65] The transfer function accounts for the scattering and absorption of the excitation light and emitted light at wavelengths λ_x and λ_m, respectively. It also accounts for the specific light illumination/collection geometry used to make the fluorescence measurements from tissues in vivo.

Figure 20 shows the computed fluorescence emission spectra of normal and adenomatous colon tissue versus the corresponding average fluorescence emission spectra measured from tissues in vivo. The peak intensity of the in vivo spectra has been scaled for comparison. The computed spectra contain all the characteristic spectral features observed in the in vivo spectra. The following interpretations may be made from the intrinsic fluorescent microstructures, the fluorescence density function and the transfer function used to calculate the computed fluorescence emission spectra shown in Figure 20:

- Although the intrinsic fluorescence of collagen (the dominant fluorophore) peaks at 420 nm, the observed peak in both normal tissues and adenoma is at 460 nm
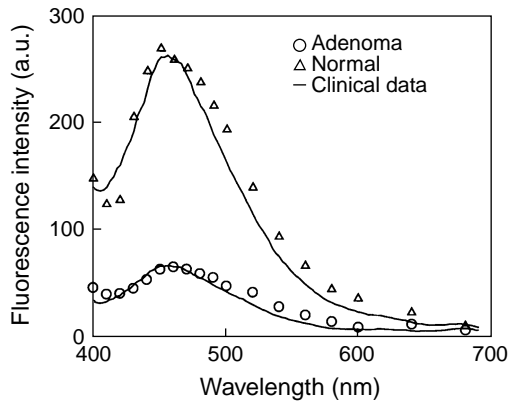
Figure 20 Computed fluorescence emission spectra from normal colon tissues and adenomas versus the average fluorescence spectra measured in vivo. (Reproduced by permission of IEEE, Piscataway, NJ (© 1996 IEEE), from Zonios et al.[82])

due to the effect of large hemoglobin absorption at 420 nm.

- The fluorescence intensity of adenoma is smaller than that of normal colon. This is due to three factors: the mucosal collagen fluorescence is decreased in adenoma due to the enlargement of crypts, which displace the lamina propria; the submucosa contributes to the fluorescence in normal tissue but not in adenoma, because of the increased thickness of a polyp; and adenoma exhibits increased absorption due to hemoglobin content.

- Red fluorescence is increased in adenoma. This additional red fluorescence is primarily associated with the intrinsic fluorescence of the dysplastic crypt cells.

In conclusion, the model developed by Zonios et al.[52] quantifies the contribution of the fluorescent microstructures that are responsible for differences observed in the fluorescence emission spectra of normal and adenomatous colon tissues. Their findings indicate that both the biochemical and morphological features of the tissue contribute to the measured fluorescence emission spectrum.

Zeng et al.[149] have used a similar approach to reconstruct in vivo skin fluorescence emission spectra. Specifically, they measured the fluorescence emission and diffuse reflectance spectra of skin in vivo and the fluorescence of the microstructures in the skin in vitro. They reconstructed the spectra measured from skin in vivo using Monte-Carlo simulations in which they used the microscopic fluorophore distribution and spectra measured from excised skin tissue sections in vitro. The optical properties of skin, however, were obtained from published values in the literature. They did not report similar data for any skin lesions such as naevi or melanoma.

7.3 Effect of Excitation and Emission Geometry on Fluorescence Emission Spectra of Turbid Media

Several groups have evaluated the effect of the excitation and emission geometry on the measurement of tissue fluorescence emission spectra from turbid media and tissue.[58,150–153] Keijzer et al.[58] used Monte-Carlo simulations and experimental measurements to show that the illumination/collection geometry affects both the intensity and line shape of fluorescence emission measured from tissue. Specifically, they demonstrated that as the separation between the illumination and collection fiber is increased, the measured fluorescence intensity decreases as a result of hemoglobin absorption. Furthermore, the attenuation due to hemoglobin absorption is wavelength dependent, thus affecting the fluorescence line shape as well. Richards-Kortum et al.[57] suggested using a fiber-optic probe, which collects the emitted light from an area, that is directly illuminated by the excitation light in order to minimize the effect of hemoglobin absorption on the fluorescence measurement. Qu et al.[150] also used Monte-Carlo simulations and experimental measurements to demonstrate that the distortion to the fluorescence emission spectrum is a function of the diameter of the area viewed by the illumination and collection fiber as well. Using bronchial tissue optical properties (for the excitation and emitted light) in their Monte-Carlo simulations, they found that the distortions to the fluorescence emission spectrum were minimized when the diameter of the tissue area viewed by the excitation and emission fiber was less than 1 mm. This was verified experimentally.

Pogue et al.[151] went a step further and demonstrated that if fluorescence is measured from a sample volume that is smaller than the average mean free scattering path (inverse of the reduced scattering coefficient) within that turbid medium, then the effects of absorption will be diminished. To achieve this, they used a confocal detection scheme to measure fluorescence as a function of fluorophore concentration from a turbid medium. They used a pinhole detector with a diameter (10 µm) that was an order of magnitude smaller than the mean free scattering path in the medium. Using this method, they were able to obtain a linear relationship between the fluorescence intensity and concentration of the fluorophore in the turbid medium for a wide range of fluorophore concentrations. Although this relationship was independent of the absorption coefficient, the fluorescence intensity varied linearly with the scattering coefficient for a fixed fluorophore concentration. Fortuitously, this is not a serious limitation because most tissues do not have a large variation in their scattering coefficient. It was also observed

for a fixed detector size that, as the mean free scattering path decreases, the number of nonscattered fluorescent photons relative to the number of scattered fluorescent photons that are detected also decreases. This suggests that the size of the detector has to be reduced as the mean free scattering path length of the turbid medium is reduced. This has direct implications on the strength of the fluorescence intensities detected and the size of the sampled volume. In a subsequent report, Pogue et al.[152] showed that they could overcome the problem of poor signal-to-noise ratio by developing and employing a fiber-optic probe that has multiple fibers (100 μm in diameter), each of which serves as an independent source and detector. Using this probe, the fluorescence intensity measured by each fiber was obtained from a sample volume smaller than the mean free scattering path for that medium, thus minimizing the effect of absorption. By integrating the fluorescence intensity from a total of 30 fibers, the signal-to-noise ratio of the fluorescence measurements was enhanced significantly. The main limitation of this technique is the very small sampled volume.

Avrillier et al.[153] used an alternative approach to resolve the effect of the illumination/collection geometry on the fluorescence emission spectra of tissue. They used Monte-Carlo simulations and optical properties of tissues measured in vitro to predict the effect of absorption and scattering on the tissue fluorescence emission spectra measured in vivo. Specifically, they predicted the correction factors as a function of increased separation between the excitation and emission fibers. These predictions were used to correct the distortion in the fluorescence emission spectra measured from the tissues. However, because the optical properties of tissues measured in vitro are fraught with error associated with extraction, this approach is considered to be, at best, approximate unless the tissue optical properties used in the Monte-Carlo simulations are measured in vivo.

8 FUTURE PERSPECTIVES

Diagnostic tools based on optical spectroscopy in the UV/VIS spectral regions have the potential to link the biochemical and morphological properties of tissues to individual patient care. In particular, these techniques are fast, noninvasive and quantitative. Furthermore, the accuracy and efficacy of the technology have been demonstrated clinically to be comparable or superior to current clinical modalities.

However, the biochemical and morphological basis for the diagnostic capability of fluorescence spectroscopy is not completely understood. This is limited by the lack of: sophisticated mathematical models that can be used to quantify tissue optical properties in order to account for the effects of absorption and scattering in the UV/VIS spectral region; and a comprehensive understanding of the biochemical constituents that contribute to the measured fluorescence. Hence, today's challenge for biomedical optics is to elucidate tissue biochemistry and morphology in greater detail for the specific disease process so that appropriate therapeutic interventions may have the greatest impact. In order to achieve this, both experimental and mathematical techniques need to developed that can enable a greater understanding of the chromophores and fluorophores that are modulated by the disease process and their contribution to the measured spectrum.

Animal models are useful with regard to developing methodologies that can be used to elucidate the biochemical and morphological properties of tissue and optimizing the instruments to exploit these features. The advantages that they offer are: they are well characterized; spectral measurements can be made per tissue site for a variety of experimental and biological conditions; and data can be obtained from a statistically significant number of animals for the purpose of validation without the need for expensive clinical trials. Although animal model studies have been performed extensively in relation to the use of photosensitizing agents for PDT, only a handful of studies on measuring and quantifying tissue autofluorescence have been performed.[154–159]

With respect to clinical applications, the diagnostic potential of fluorescence spectroscopy is defined by histology. In order to evaluate if fluorescence spectroscopy is sensitive to changes that precede the morphological manifestations seen by histological evaluation, it is valuable to correlate the measured spectral information to other biochemical and/or genetic markers of increased cancer risk. Furthermore, although fluorescence spectroscopy has been most widely explored for the detection of precancer or cancer in a screening and diagnostic setting, its diagnostic potential for guiding surgery has been evaluated only in a limited number of clinical studies.[101] Because this technique can discriminate between diseased and nondiseased tissues in a fast and noninvasive manner, it could be used to define margins of resection for various surgical procedures, such as that of the breast and brain. Additionally, this technique also could be used to monitor the response of tissues to various therapeutic interventions.

ABBREVIATIONS AND ACRONYMS

APD	Avalanche Photodiode
ATP	Adenosine Triphosphate
BPD	Benzoporphyrin Derivative
CCD	Charge-coupled Device
EEM	Excitation–Emission Matrix
FAD	Flavin Adenine Dinucleotide
$FADH_2$	Reduced Flavin Adenine Dinucleotide
Fp	Flavoprotein
fwhm	Full Width at Half-maximum
HpD	Hematoporphyrin Derivative
IR	Infrared
LIFE	Light-induced Fluorescence Endoscopy
MTHPC	Meso-tetra-(hydroxyphenyl)-chlorin
NAD^+	Nicotinamide Adenine Dinucleotide
NADH	Reduced Nicotinamide Adenine Dinucleotide
NIR	Near-infrared
NIST	National Institute of Standards and Technology
PCA	Principal Component Analysis
PDA	Photodiode Array
PDT	Photodynamic Therapy
PLS	Partial Least Squares
PMT	Photomultiplier Tube
PN	Pyridine Nucleotide
PpIX	Protoporphyrin IX
SIL	Squamous Intra-epithelial Lesions
SnET2	Tin Etiopurpurin
UV	Ultraviolet
VIS	Visible
5-ALA	δ-Aminolevulinic Acid

RELATED ARTICLES

Biomedical Spectroscopy **(Volume 1)**
Biomedical Spectroscopy: Introduction • Infrared Spectroscopy in Clinical and Diagnostic Analysis • Infrared Spectroscopy, Ex Vivo Tissue Analysis by • Near-infrared Spectroscopy, In Vivo Tissue Analysis by • Photodynamic Therapy

REFERENCES

1. R.S. Cotran, V. Kumar, S.L. Robbins, *Robbins Pathologic Basis of Disease*, WB Saunders Co., Philadelphia, PA, 1989.
2. I.D. Campbell, R.A. Dwek, *Biological Spectroscopy*, Benjamin/Cummings Publishing Co., Menlo Park, CA, 1984.
3. F. Koenig, F.J. McGovern, H. Enquist, R. Larne, T.F. Deutsch, K.T. Schomacker, 'Autofluorescence Guided Biopsy for the Early Diagnosis of Bladder Carcinoma', *J. Urol.*, **159**(6), 1871–1875 (1998).
4. B. Chance, M. Cope, B. Dugan, N. Ramanujam, B. Tromberg, 'Phase Measurements of Absorbers and Scatterers in Tissue: Review', *Rev. Sci. Instrum.*, **69**(10), 3457–3481 (1998).
5. S. Andersson-Engels, J. Johansson, U. Stenram, K. Svanberg, S. Svanberg, 'Malignant Tumor and Atherosclerotic Plaque Diagnosis Using Laser Induced Fluorescence', *IEEE J. Quant. Electron.*, **26**(12), 2207–2217 (1990).
6. S. Andersson-Engels, J. Johansson, K. Svanberg, S. Svanberg, 'Fluorescence Imaging and Point Measurements of Tissue: Applications to the Demarcation of Malignant Tumors and Atherosclerotic Lesions from Normal Tissue', *Photochem. Photobiol.*, **53**(6), 807–814 (1991).
7. S. Andersson-Engels, B.C. Wilson, 'In Vivo Fluorescence in Clinical Oncology: Fundamentals and Practical Issues', *J. Cell. Pharmacol.*, **3**, 66–79 (1992).
8. T.G. Papazoglou, 'Malignancies and Atherosclerotic Plaque Diagnosis – Is Laser Induced Fluorescence Spectroscopy the Ultimate Solution?', *J. Photochem. Photobiol. B: Biol.*, **28**, 3–11 (1995).
9. I.J. Bigio, J.R. Mourant, 'Ultraviolet and Visible Spectroscopies for Tissue Diagnostics: Fluorescence Spectroscopy and Elastic-scattering Spectroscopy', *Phys. Med. Biol.*, **42**, 803–814 (1996).
10. S. Andersson-Engels, C.A. Klinteberg, K. Svanberg, S. Svanberg, 'In Vivo Fluorescence Imaging for Tissue Diagnostics', *Phys. Med. Biol.*, **42**, 815–824 (1997).
11. R. Richards-Kortum, E. Sevick-Muraca, 'Quantitative Optical Spectroscopy for Tissue Diagnosis', *Annu. Rev. Phys. Chem.*, **47**, 555–606 (1996).
12. G.A. Wagnieres, W.M. Star, B.C. Wilson, 'In Vivo Fluorescence Spectroscopy and Imaging for Oncological Applications', *Photochem. Photobiol.*, **68**(5), 603–632 (1998).
13. E.B. Hanlon, I. Itzkan, R.R. Dasari, M.S. Feld, R.J. Ferrante, A.C. McKee, D. Lathi, N.W. Kowall, 'Near-infrared Fluorescence Spectroscopy Detects Alzheimer's Disease In Vitro', *Photochem. Photobiol.*, **70**(2), 236–242 (1999).
14. L.T. Perelman, V. Backman, M. Wallace, G. Zonios, R. Manoharan, A. Nusrat, S. Shields, M. Seiler, C. Lima, T. Hamano, I. Itzkan, J. Van Dam, J.M. Crawford, M.S. Feld, 'Observation of Periodic Fine Structure in Reflectance from Biological Tissue: a New Technique for Measuring Nuclear Size Distribution', *Phys. Rev. Lett.*, **80**(3), 627–630 (1998).
15. B.B. Das, F. Liu, R.R. Alfano, 'Time-resolved Fluorescence and Photon Migration Studies in Biomedical

and Random Media', *Rep. Prog. Phys.*, **60**(2), 227–292 (1997).

16. S.P. Gopinath, C.S. Robertson, R.G. Grossman, B. Chance, 'Near-infrared Spectroscopic Localization of Intracranial Hematomas', *J. Neurosurg.*, **79**, 43–47 (1993).

17. W.J. Levy, S. Levin, B. Chance, 'Near-infrared Measurement of Cerebral Oxygenation: Correlation with Electroencephalographic Ischemia During Ventricular Fibrillation', *Anesthesiology*, **83**(4), 738–746 (1995).

18. S. Nioka, Q. Luo, B. Chance, 'Human Brain Functional Imaging with Reflectance CWS', *Adv. Exp. Med. Biol.*, **428**, 237–242 (1997).

19. A. Villringer, B. Chance, 'Non-invasive Optical Spectroscopy and Imaging of Human Brain Function', *Trends Neurosci.*, **20**(10), 435–442 (1997).

20. W. Bank, B. Chance, 'Diagnosis of Defects in Oxidative Muscle Metabolism by Non-invasive Tissue Oximetry', *Mol. Cell. Biochem.*, **174**(1/2), 7–10 (1997).

21. S. Nioka, M. Miwa, S. Orel, M. Shnall, M. Haida, S. Zhao, B. Chance, 'Optical Imaging of Human Breast Cancer', *Adv. Exp. Med. Biol.*, **361**, 171–179 (1994).

22. D.A. Boas, A.G. Yodh, 'Spatially Varying Dynamical Properties of Turbid Media Probed with Diffusing Temporal Light Correlation', *J. Opt. Soc. Am. A*, **14**, 192–215 (1997).

23. A. Mahadevan-Jansen, R. Richards-Kortum, 'Raman Spectroscopy of Pre-cancers and Cancers', *J. Biomed. Opt.*, **1**(1), 31–70 (1996).

24. J.F. Brennan III, M.E. Beattie, Y. Wang, M.J. Cantella, B.Y. Tsaur, R.R. Dasari, M.S. Feld, 'PdSi Focal-plane Array Detectors for Short-wave Infrared Raman Spectroscopy of Biological Tissue: a Feasibility Study', *Appl. Opt.*, **35**(28), 5736–5739 (1996).

25. A.J. Berger, T.W. Koo, I. Itzkan, G. Horowitz, M.S. Feld, 'Multicomponent Blood Analysis by Near-infrared Raman Spectroscopy', *Appl. Opt.*, **38**(13), 2916–2926 (1999).

26. J.R. Lakowicz, *Principles of Fluorescence Spectroscopy*, Plenum Press, New York, 1983.

27. M.B. Silberberg, H.E. Savage, G.C. Tang, P.G. Sacks, R.R. Alfano, S.P. Schantz, 'Detection of Retinoic Acid Induced Biochemical Alterations in Squamous Cell Carcinoma Using Intrinsic Fluorescence Spectroscopy', *Laryngoscopy*, **104**(3), 278–282 (1994).

28. A. Pradhan, P. Pal, G. Durocher, L. Villeneuve, A. Balassy, F. Babai, L. Gaboury, L. Blanchard, 'Steady State and Time Resolved Fluorescence Properties of Metastatic and Non-metastatic Malignant Cells from Different Species', *J. Photochem. Photobiol. B: Biol.*, **3**(3), 101–112 (1995).

29. S. Ganesan, P.G. Sacks, Y. Yang, A. Katz, M. Al-Rawi, H.E. Savage, S.P. Schantz, R.R. Alfano, 'Native Fluorescence Spectroscopy of Normal and Malignant Epithelial Cells', *Cancer Biochem. Biophys.*, **16**, 365–373 (1998).

30. T.J. Romer, M. Fitzmaurice, R.M. Cothren, R. Richards-Kortum, M.V. Sivak, Jr, J.R. Kramer, Jr, 'Laser-induced Fluorescence Microscopy of Normal Colon and Dysplasia in Colonic Adenomas: Implications for Spectroscopic Diagnosis', *Am. J. Gastroenterol.*, **90**(1), 81–87 (1995).

31. H. Wang, J. Willis, M.J.F. Canto, M.V. Sivak, Jr, J.A. Izatt, 'Quantitative Laser Scanning Confocal Autofluorescence Microscopy of Normal, Premalignant, and Malignant Colonic Tissues', *IEEE Trans. Biomed. Eng.*, **46**(10), 1246–1252 (1999).

32. G.S. Fairman, M.H. Nathanson, A.B. West, L.I. Deckelbaum, L. Kelly, C.R. Kapadia, 'Differences in Laser-induced Autofluorescence Between Adenomatous and Hyperplastic Polyps and Normal Colonic Mucosa by Confocal Microscopy', *Digest. Dis. Sci.*, **40**(6), 1261–1268 (1995).

33. K. Izuishi, H. Tajiri, T. Fujii, N. Boku, A. Ohtsu, T. Ohnishi, M. Ryi, T. Kinoshita, S. Yoshida, 'The Histological Basis of Detection of Adenoma and Cancer in the Colon by Autofluorescence Endoscopic Imaging', *Endoscopy*, **31**(7), 511–516 (1999).

34. G. Bottiroli, A.C. Croce, D. Locatelli, R. Marchesini, E. Pignoli, S. Tomatis, C. Cuzzoni, S. Di Palma, M. Dalfante, P. Spinellu, 'Natural Fluorescence of Normal and Neoplastic Human Colon: a Comprehensive "ex vivo" Study', *Lasers Surg. Med.*, **16**(1), 48–60 (1995).

35. G.I. Zonios, R.M. Cothren, J.T. Arendt, J. Wu, J. Van Dam, J.M. Crawford, R. Manoharan, M.S. Feld, 'Morphological Model of Human Colon Tissue Fluorescence', *IEEE Trans. Biomed. Eng.*, **43**(2), 113–122 (1996).

36. R.S. DaCosta, L. Ligle, J. Kost et al., 'Confocal Microscopy/Macroscopy and Microspectrofluorimetry Analysis of Human Colorectal Tissue', *J. Anal. Morphol.*, **4**, 192–194 (1997).

37. W.S. Glassman, M. Steinberg, R.R. Alfano, 'Time Resolved and Steady State Fluorescence Spectroscopy from Normal and Malignant Cultured Human Breast Cell Lines', *Lasers Life Sci.*, **6**(2), 91–98 (1994).

38. M. Anidjar, O. Cussenot, J. Blais, O. Bourdon, S. Avrillier, D. Ettori, J.M. Villter, J. Fiet, P. Teillac, A. Le Duc, 'Argon Laser Induced Autofluorescence may Distinguish Between Normal and Tumor Human Urothelial Cells: a Microspectrofluorimetric Study', *J. Urol.*, **155**(5), 1771–1774 (1996).

39. F.N. Ghadially, W.J.P. Neish, H.C. Dawkins, 'Mechanisms Involved in the Production of Red Fluorescence of Human and Experimental Tumors', *J. Pathol. Bacteriol.*, **85**, 77–92 (1963).

40. L. Stryer, *Biochemistry*, WH Freeman and Company, New York, 1988.

41. D. Fujimoto, 'The Structure of Pyridinoline, a Collagen Crosslink', *Biochem. Biophys. Res. Commun.*, **76**(4), 1124–1129 (1977).

42. Z. Deyl, K. Macek, M. Adam, O. VanCikova, 'Studies on the Chemical Nature of Elastin Fluorescence', *Biochim. Biophys. Acta*, **625**, 248–254 (1980).

43. D.R. Eyre, M.A. Paz, 'Cross-linking in Collagen and Elastin', *Annu. Rev. Biochem.*, **53**, 717–748 (1984).

44. D.P. Thornhill, 'Separation of a Series of Chromophores and Fluorophores Present in Elastin', *Biochem. J.*, **147**, 215–219 (1975).

45. B. Chance, B. Schoener, R. Oshino, F. Itshak, Y. Nakase, 'Oxidation–Reduction Ratio Studies of Mitochondria in Freeze-trapped Samples', *J. Biol. Chem.*, **254**(11), 4764–4771 (1979).

46. A.M. Kluftinger, N.L. Davis, N.F. Quenville, S. Lam, J. Hung, B. Palcic, 'Detection of Squamous Cell Cancer and Pre-cancerous Lesions by Imaging Tissue Autofluorescence in the Hamster Cheek Pouch Model', *Surg. Oncol.*, **1**, 183–188 (1992).

47. A. Policard, 'Etudes sur les Aspects Offerts par des Tumeurs Experimentales Examinees a la Lumiere de Woods', *CR Soc. Biol.*, **91**, 1423–1425 (1924).

48. F. Ronchese, 'The Fluorescence of Cancer Under the Wood's Light', *Oral Surg. Oral Med. Pathol.*, **7**, 967–971 (1954).

49. F.N. Ghadially, 'Red Fluorescence of Experimentally Induced and Human Tumors', *J. Pathol. Bacteriol.*, **80**, 345–361 (1960).

50. F.N. Ghadially, W.J.P. Neish, 'Porphyrin Fluorescence of Experimentally Induced Squamous Cell Carcinoma', *Nature*, **188**, 1124 (1960).

51. F.N. Ghadially, W.J.P. Neish, H.C. Dawkins, 'Mechanisms Involved in the Production of Red Fluorescence of Human and Experimental Tumors', *J. Pathol. Bacteriol.*, **85**, 77–92 (1963).

52. J.C. Kennedy, R.H. Pottier, D.C. Pross, 'Photodynamic Therapy with Endogenous Protoporphyrin IX: Basic Principles and Present Clinical Experience', *J. Photochem. Photobiol. B*, **6**, 143–148 (1990).

53. W.F. Cheong, A.J. Welch, 'A Review of the Optical Properties of Tissues', *IEEE J. Quantum Electron.*, **26**, 2166–2185 (1990).

54. R. Richards-Kortum, 'Fluorescence Spectroscopy of Turbid Media', in *Optical–Thermal Response of Laser Irradiated Tissue*, eds. A.J. Welch, M.J.C. van Gemert, Plenum Press, New York, 667–706, 1995.

55. S.B. Brown, *An Introduction to Spectroscopy for Biochemists*, Academic Press, London, 1980.

56. A.J. Durkin, S. Jaikumar, N. Ramanujam, R. Richards-Kortum, 'Relation Between Fluorescence Spectra of Dilute and Turbid Samples', *Appl. Opt.*, **33**(3), 414 (1994).

57. R. Richards-Kortum, A. Mehta, G. Hayes, R. Cothren, T. Kolubayev, C. Kitrell, N.B. Ratliff, J.R. Kramer, M.S. Feld, 'Spectral Diagnosis of Atherosclerosis Using an Optical Fiber Laser Catheter', *Am. Heart J.*, **118**(2), 381 (1989).

58. M. Keijzer, R. Richards-Kortum, S.L. Jacques, M.S. Feld, 'Fluorescence Spectroscopy of Turbid Media: Autofluorescence of the Human Aorta', *Appl. Opt.*, **28**, 4286–4292 (1989).

59. S. Chandrasekhar, *Radiative Transfer*, Oxford University Press, Oxford, 1950.

60. A. Ishimaru, *Wave Propagation and Scattering in Random Media*, Academic Press, New York, 1987.

61. P. Kubelka, 'New Contributions to the Optics of Intensely Light Scattering Materials. Part II: Non-homogeneous Layers', *J. Opt. Soc. Am.*, **344**, 330–335 (1954).

62. S. Prahl, M.J.C. van Gemert, A.J. Welch, 'Determining the Optical Properties of Turbid Media by Using the Adding–Doubling Method', *Appl. Opt.*, **32**, 559–568 (1993).

63. M.S. Patterson, B. Chance, B.C. Wilson, 'Time Resolved Reflectance and Transmittance for the Non-invasive Measurement of Tissue Optical Properties', *Appl. Opt.*, **28**, 2331–2336 (1989).

64. J.J. Duderstadt, L.J. Hamilton, *Nuclear Reactor Analysis*, Wiley, New York, 103–144, 1976.

65. S.L. Jacques, 'Monte-Carlo Methods', in *Optical–Thermal Response of Laser-irradiated Tissue*, eds. A.J. Welch, M.J.C. van Gemert, Plenum Press, New York, 73–99, 1995.

66. A.J. Durkin, S. Jaikumar, R. Richards-Kortum, 'Optically Dilute, Absorbing and Turbid Phantoms for Fluorescence Spectroscopy of Homogeneous and Inhomogeneous Samples', *Appl. Spectrosc.*, **47**, 2114–2121 (1993).

67. G. Wagnieres, S. Cheng, M. Zellweger, N. Utke, D. Braichotte, J.-P. Ballini, H. van den Bergh, 'An Optical Phantom with Tissue-like Properties in the Visible for Use in PDT and Fluorescence Spectroscopy', *Phys. Med. Biol.*, **42**(7), 1415–1426 (1997).

68. E. Kohen, R. Santus, J.G. Hirschberg, *Photobiology*, Academic Press, San Diego, CA, 1995.

69. R.A. Zangaro, L. Silveira, R. Manoharan, G. Zonios, I. Itzkan, R.R. Dasari, J. Van Dam, M.S. Feld, 'Rapid Multi-excitation Fluorescence Spectroscopy System for In Vivo Tissue Diagnosis', *Appl. Opt.*, **35**(25), 5211–5219 (1996).

70. R.L. McCreery, 'CCD Array Detectors for Multi-channel Raman Spectroscopy', in *Charged Transfer Devices in Spectroscopy*, eds. J.V. Sweedler, K.L. Ratzlaff, M.B. Denton, VCH Publishers, New York, 227–279, 1994.

71. E.V. Trujillo, D.R. Sandison, U. Utzinger, N. Ramanujam, M. Follen Mitchell, R. Richards-Kortum, 'Method to Determine Tissue Fluorescence Efficiency In Vivo and Predict Signal-to-noise Ratio for Spectrometers', *Appl. Spectrosc.*, **52**(7), 943–951 (1998).

72. D.G. Taylor, J.N. Demas, *Anal. Chem.*, **51**, 712 (1979).

73. G.G. Stokes, 'Uber Die Anderung der Brechbarkeit des Lichtes', *Philos. Trans. R. Soc.*, **107**, 11 (1852).

74. H. Stubel, 'Die Fluoreszenz Tierischer Gewebe in Ultravioletten Licht', *Pflugers Arch. Physiol.*, **142**, 1 (1911).

75. R.M. Lycette, R.B. Leslie, *Lancet*, **2**, 436 (1965).

76. A.E. Profio Profio, D.R. Doiron, E.G. King, 'Laser Fluorescence Bronchoscope for Localization of Occult Lung Tumors', *Med. Phys.*, **6**(6), 523–525 (1979).

77. A.E. Profio, D.R. Doiron, 'A Feasibility Study of the Use of Fluorescence Bronchoscopy for the Localization of Small Lung Tumors', *Phys. Med. Biol.*, **22**, 949–957 (1977).

78. R.R. Alfano, D.B. Tata, J. Cordero, P. Tomashefsky, F.W. Longo, M.A. Alfano, 'Laser Induced Fluorescence Spectroscopy from Native Cancerous and Normal Tissue', *IEEE J. Quant. Electron.*, **20**, 1507–1511 (1984).

79. W. Lohmann, 'In Situ Detection of Melanomas by Fluorescence Measurements', *Maturwissenschaften*, **75**, 201–202 (1988).

80. Y. Yang, Y. Ye, F. Li, Y. Li, P. Ma, 'Characteristic Autofluorescence for Cancer Diagnosis and its Origin', *Lasers Surg. Med.*, **7**, 528–532 (1987).

81. A. Mahadevan, M.F. Mitchell, E. Silva, S. Thomsen, R. Richards-Kortum, 'A Study of the Fluorescence Properties of Normal and Neoplastic Human Cervical Tissue', *Lasers Surg. Med.*, **13**, 647–655 (1994).

82. G.I. Zonios, R.M. Cothren, J.T. Arendt, J. Wu, J. Van Dam, J.M. Crawford, R. Manoharan, M.S. Feld, 'Morphological Model of Human Colon Tissue Fluorescence', *IEEE Trans. Biomed. Eng.*, **43**, 113–122 (1996).

83. K.T. Schomacker, J.K. Frisoli, C.C. Compton, T.J. Flotte, J.M. Richter, N.S. Nishioka, T.F. Deutsch, 'Ultraviolet Laser-induced Fluorescence of Colonic Tissue: Basic Biology and Diagnostic Potential', *Lasers Surg. Med.*, **12**(1), 63–78 (1992).

84. C. Eker, S. Montan, E. Jaramillo, K. Koizumi, C. Rubio, S. Andersson-Engels, K. Svanberg, S. Svanberg, P. Slezak, 'Clinical Spectral Characterization of Colonic Mucosal Lesions Using Autofluorescence and Delta Amniolevulinic Acid Sensitization', *Gut*, **44**(4), 511–518 (1999).

85. R.M. Cothren, M.V. Sivak, J. Van Dam, R.E. Petras, M. Fitzmaurice, J.M. Crawford, J. Wu, J.F. Brennan, R.P. Rava, R. Manoharan, M.S. Feld, 'Detection of Dysplasia at Colonoscopy Using Laser Induced Fluorescence: a Blinded Study', *Gastrointest. Endosc.*, **44**(2), 168–176 (1996).

86. T.D. Wang, J.M. Crawford, M.S. Feld, Y. Wang, I. Itzkan, J. Van Dam, 'In Vivo Identification of Colonic Dysplasia Using Fluorescence Endoscopic Imaging', *Gastrointest. Endosc.*, **49**(4), 447–455 (1999).

87. M.A. Mycek, K.T. Schomacker, N.S. Nishioka, 'Colonic Polyp Differentiation Using Time-resolved Autofluorescence Spectroscopy', *Gastrointest. Endosc.*, **48**(4), 390–394 (1998).

88. N. Ramanujam, M.F. Mitchell, A. Mahadevan-Jansen, S. Thomsen, G. Staerkel, A. Malpica, T. Wright, A. Atkinson, R. Richards-Kortum, 'Cervical Pre-cancer Detection Using a Multivariate Statistical Algorithm Based on Laser Induced Fluorescence Spectra at Multiple Excitation Wavelengths', *Photochem. Photobiol.*, **64**, 720–735 (1996).

89. K. Tumer, N. Ramanujam, J. Ghosh, R. Richards-Kortum, 'Ensembles of Radial Basis Function Networks for Spectroscopic Detection of Cervical Precancer', *IEEE Trans. Biomed. Eng.*, **45**(8), 953–961 (1998).

90. S. Lam, T. Kennedy, M. Unger, Y.E. Miller, D. Gelmont, V. Rusch, B. Gipe, D. Howard, J. LeRiche, A. Coldman, A. Gazdar, 'Localization of Bronchial Intraepithelial Neoplastic Lesions by Fluorescence Bronchoscopy', *Chest*, **113**(3), 696–702 (1998).

91. F. Koenig, F.J. McGovern, A.F. Althausen, T.F. Deutsch, K.T. Schomacker, 'Laser Induced Autofluorescence Diagnosis of Bladder Cancer', *J. Urol.*, **156**(5), 1597–1601 (1996).

92. M. Anidjar, D. Ettori, O. Cussenot, P. Meria, F. Desgrandchamps, A. Cortesse, P. Teillac, A. Le Duc, S. Avrillier, 'Laser Induced Autofluorescence of Bladder Tumors: Dependence on Excitation Wavelength', *J. Urol.*, **156**(5), 1590–1596 (1996).

93. M. Panjehpour, B.F. Overholt, T. Vo-Dinh, R.C. Haggit, D.H. Edwards, F.P. Buckely III, 'Endoscopic Fluorescence Detection of High Grade Dysplasia in Barrett's Esophagus', *Gastroenterology*, **111**, 93–101 (1996).

94. J.K. Dhingra, D.F. Perrault, K. McMillan, E.E. Rebeiz, S. Kabani, R. Manoharan, I. Itzkan, M.S. Feld, S.M. Shapshay, 'Early Diagnosis of Upper Aerodigestive Tract Cancer by Autofluorescence', *Arch. Otolaryngol. – Head Neck Surg.*, **122**(11), 1181–1186 (1996).

95. A. Gillenwater, R. Jacob, R. Ganeshappa, B. Kemp, A.K. El-Naggar, J.L. Palmer, G. Clayman, M.F. Mitchell, R. Richards-Kortum, 'Noninvasive Diagnosis of Oral Neoplasia Based on Fluorescence Spectroscopy and Native Tissue Autofluorescence', *Arch. Otolaryngol. – Head Neck Surg.*, **124**(11), 1251–1258 (1998).

96. B. Kulapaditharom, V. Boonkitticharoan, 'Laser Induced Fluorescence Imaging in Localization of Head and Neck Cancers', *Ann. Otol. Rhinol. Laryngol.*, **107**(3), 241–246 (1998).

97. C.S. Betz, M. Mehlmann, K. Rick, H. Stepp, G. Grevers, R. Baumgartner, A. Leunig, 'Autofluorescence Imaging and Spectroscopy of Normal and Malignant Mucosa in Patients with Head and Neck Cancer', *Lasers Surg. Med.*, **25**, 323–334 (1999).

98. M.L. Harries, S. Lam, C. MacAulay, J.A. Qu, B. Palcic, 'Diagnostic Imaging of the Larynx: Autofluorescence of Laryngeal Tumors Using the Helium Cadmium Laser', *J. Laryngol. Otol.*, **109**, 108–110 (1995).

99. M. Zargi, L. Smid, I. Fajdiga, B. Bubnic, J. Lenarcic, P. Oblak, 'Laser Induced Fluorescence in Diagnostics of Laryngeal Cancer', *Acta Oto-Laryngol. Suppl.*, **527**, 125–127 (1997).

100. B.W. Chwirot, S. Chwirot, J. Redzinski, Z. Michiniewicz, 'Detection of Melanomas by Digital Imaging of

Spectrally Resolved Ultraviolet Light Induced Autofluorescence of Human', *Eur. J. Cancer*, **34**(11), 1730–1734 (1998).

101. G. Bottiroli, A.C. Croce, D. Locatelli, R. Nano, E. Giombelli, A. Messina, E. Benericetti, 'Brain Tissue Autofluorescence: an Aid for Intra-operative Delineation of Tumor Resection Margins', *Cancer Detect. Prevent.*, **22**(4), 330–339 (1998).

102. K. Izuishi, H. Tajiri, M. Ryu, J. Furuse, Y. Maru, K. Inoue, M. Konishi, T. Kinoshita, 'Detection of Bile Duct Cancer by Autofluorescence Cholangioscopy: a Pilot Study', *Hepato-Gastroenterology*, **46**(26), 804–807 (1999).

103. B.W. Chwirot, S. Chwirot, W. Jedrzejczyk, M. Jackowski, A.M. Raczynska, J. Winczakiewicz, J. Dobber, 'Ultraviolet Laser Induced Fluorescence of Human Stomach Tissues: Detection of Cancer Tissues by Imaging Techniques', *Lasers Surg. Med.*, **21**(2), 149–158 (1997).

104. R.R. Alfano, G.C. Tang, A. Pradhan, W. Lam, D.S.J. Choy, E. Opher, 'Fluorescence Spectra from Cancerous and Normal Breast and Lung Tissue', *IEEE J. Quant. Electron.*, **23**, 1806–1811 (1987).

105. Y. Yang, A. Katz, E.J. Celmer, M. Zurawska-Szczepaniak, R.R. Alfano, 'Optical Spectroscopy of Benign and Malignant Tissues', *Lasers Life Sci.*, **7**(2), 115–127 (1996).

106. Y. Yang, A. Katz, E.J. Celmer, M. Zurawska-Szczepaniak, R.R. Alfano, 'Excitation Spectrum of Malignant and Benign Breast Tissues: a Potential Optical Biopsy Approach', *Lasers Life Sci.*, **7**(4), 249–265 (1997).

107. P.K. Gupta, S.K. Majumder, A. Uppal, 'Breast Cancer Diagnosis Using Nitrogen Laser Excited Autofluorescence Spectroscopy', *Lasers Surg. Med.*, **21**(5), 417–422 (1997).

108. H. Auler, G. Banzer, 'Untersuchungen uber die Rolle der Porphine bei Geschwulstkranken Menschen und Tieren', *Krebforschung*, **53**, 1423–1425 (1942).

109. R.H. Figge, 'Near Ultraviolet Rays and Fluorescence Phenomena as Aids to Discovery and Diagnosis in Medicine', *Univ. Md. Med. Bull.*, **26**, 165–168 (1942).

110. G.E. Moore, W.T. Peyton, L.A. French, W.W. Walker, 'The Clinical Use of Fluorescin in Neurosurgery', *J. Neurosurg.*, **5**, 392–398 (1948).

111. G.C. Peck, H.P. Mack, H.F. Figge, 'Cancer Detection and Therapy III. Affinity of Lymphatic Tissues for Hematoporphyrin', *Bull. School Med. Univ. Md.*, **38**, 124–127 (1953).

112. G.C. Peck, H.P. Mack, W.A. Holbrook, H.F. Figge, 'Use of Hematoporphyrin Fluorescence in Biliary and Cancer Surgery', *Bull. School Med. Univ. Md.*, **38**, 124–127 (1955).

113. D.S. Rassmussen-Taxdal, G.R. Ward, F.H. Figge, 'Fluorescence of Human Lymphatic and Cancer Tissue Following High Doses of Intravenous Hematoporphyrin', *Cancer*, **8**, 78–81 (1958).

114. R.L. Lipson, E.J. Baldes, A.M. Olsen, 'Haematoporphyrin Derivative: a New Aid for Endoscopic Detection of Malignant Disease', *J. Thorac. Cardiovasc. Surg.*, **42**, 623–629 (1961).

115. R.L. Lipson, E.J. Baldes, A.M. Olsen, 'The Use of a Derivative of Haematoporphyrin in Tumor Detection', *J. Natl. Cancer Inst.*, **26**, 1–11 (1961).

116. R.L. Lipson, E.J. Baldes, A.M. Olsen, 'A Further Evaluation of the Use of Haematoporphyrin Derivative as a New Aid for Endoscopic Detection of Malignant Disease', *Dis. Chest*, **46**, 676–679 (1964).

117. R.L. Lipson, J.H. Pratt, E.J. Baldes, M.B. Dockerty, 'Haematoporphyrin Derivative for Detection of Cervical Cancer', *Obstet. Gynecol.*, **24**, 78–84 (1964).

118. R.L. Lipson, E.J. Baldes, M.J. Gray, 'Hematoporphyrin Derivative for Detection and Management of Cancer', *Cancer*, **20**, 2255–2257 (1967).

119. M.J. Gray, R.L. Lipson, J.V.S. Maeck, L. Parker, D. Romeyn, 'Use of Hematoporphyrin Derivative in Detection and Management of Cervical Cancer: a Preliminary Report', *Am. J. Obstet. Gynecol.*, **99**, 766–771 (1967).

120. H.B. Gregorie, E.O. Horger, J.L. Ward, J.R. Green, T. Richards, H.C. Robertson, T.B. Stevenson, 'Hematoporphyrin Derivative Fluorescence in Malignant Neoplasms', *Ann. Surg.*, **167**, 820–828 (1968).

121. T.B. Leonard, W.L. Beck, 'Hematoporphyrin Fluorescence: an Aid in Diagnosis of Malignant Neoplasms', *Laryngoscopy*, **81**, 365–377 (1971).

122. J.F. Kelly, J.F. Snell, 'Hematoporphyrin Derivative: a Possible Aid in the Diagnosis and Therapy of Carcinoma of the Bladder', *J. Urol.*, **115**, 150–151 (1976).

123. M. Kreigmair, R. Baumgartner, W. Lumper, R. Reisenberg, S. Stocker, A. Hofstetter, 'Fluorescence Cystoscopy Following Intravesical Instillation of 5-Aminolevulinic Acid (ALA)', *J. Urol.*, **149**, 240A (1993).

124. P. Edholm, B. Jacobson, 'Detection of Aortic Atheromatosis In Vivo by Reflection Spectrophotometry', *J. Atheroscler. Res.*, **5**, 592–595 (1965).

125. C. Kitrell, R.L. Willett, C. de los Santos-Pacheco, N.B. Ratliff, J.R. Kramer, E.G. Malk, M.S. Feld, 'Diagnosis of Fibrous Arterial Atherosclerosis Using Fluorescence', *Appl. Opt.*, **24**, 2280–2281 (1985).

126. J. Wu, M.S. Feld, R.P. Rava, 'Analytical Model for Extracting Intrinsic Fluorescence from a Turbid Media', *Appl. Opt.*, **32**(19), 3585–3595 (1993).

127. C.M. Gardner, S.L. Jacques, A.J. Welch, 'Fluorescence Spectroscopy of Tissue: Recovery of Intrinsic Fluorescence from Measured Fluorescence', *Appl. Opt.*, **35**(10), 1780–1792 (1996).

128. H. Zeng, C. MacAulay, B. Palcic, D. McLean, 'A Computerized Autofluorescence and Diffuse Reflectance Spectroanalyzer for In Vivo Skin Studies', *Phys. Med. Biol.*, **38**, 231–240 (1993).

129. A.F. Zuluaga, U. Utzinger, A.J. Durkin, F. Holger, A. Gillenwater, R. Jacob, B. Kemp, J. Fan, R. Richards-Kortum, 'Fluorescence Excitation and Emission Matrices of Human Tissues: a System for In Vivo Measurement and Method of Data Analysis', *Appl. Spectrosc.*, **53**(3), 302–311 (1999).

130. B. Palcic, S. Lam, J. Hung et al., 'Detection and Localization of Early Lung Cancer by Imaging Techniques', *Chest*, **99**, 742–743 (1991).

131. P.S. Anderson, S. Montan, T. Persson, S. Svanberg, S. Tapper, S.-E. Karlsson, 'Fluorescence Endoscopy Instrumentation for Improved Tissue Characterization', *Med. Phys.*, **14**(4), 633–636 (1987).

132. G.A. Wagnieres, A.P. Studzinski, H.E. van den Bergh, 'An Endoscopic Fluorescence Imaging System for Simultaneous Visual Examination and Photodetection of Cancers', *Rev. Sci. Instrum.*, **68**(1), 203–212 (1997).

133. T. Mckechnie, A. Jahan, I. Tait, A. Cuschieri, W. Sibbett, M. Padgett, 'An Endoscopic System for the Early Detection of Cancers of the Gastrointestinal Tract', *Rev. Sci. Instrum.*, **69**(6), 2521–2523 (1998).

134. H. Zeng, A. Weiss, R. Cline, C.E. MacAulay, 'Real-time Endoscopic Imaging for Early Cancer Detection in the Gastrointestinal Tract', *Bioimaging*, **6**(4), 151–165 (1998).

135. P.S. Andersson, S. Montan, S. Svanberg, 'Multispectral System for Medical Fluorescence Imaging', *IEEE J. Quant. Electron.*, **QE-23**(10), 1798–1805 (1987).

136. S. Andersson-Engels, J. Johansson, S. Svanberg, 'Medical Diagnostic System Based on Simultaneous Multispectral Fluorescence Imaging', *Appl. Opt.*, **34**(1), 8022–8029 (1994).

137. G.A. Duvall, J. Kost et al., 'Laser Induced Fluorescence Endoscopy (LIFE): a Pilot Study of a Real Time Autofluorescence Imaging System for Early Detection of Dysplasia and Carcinoma in the GI Tract', *Endoscopy*, **28**, S45 (1996).

138. G.A. DuVall, B.C. Wilson, N. Marcon, 'Tissue Autofluorescence', *Ann. Gastrointest. Endosc.*, **10**, 25–30 (1997).

139. R.W. Dillon, M. Goldstein, *Multivariate Analysis: Methods and Applications*, Wiley, New York, 1984.

140. A. Albert, E.K. Harris, *Multivariate Interpretation of Clinical Laboratory Data*, Marcel Dekker, New York, 1987.

141. R. Richards-Kortum, R.P. Rava, M. Fitzmaurice, J.R. Kramer, M.S. Feld, '476 nm Excited Laser Induced Fluorescence Spectroscopy of Human Coronary Artery: Applications in Cardiology', *Am. Heart J.*, **122**(4), 1141–1150 (1991).

142. D.M. Haaland, 'Multivariate Calibration Methods Applied to Quantitative Analysis of Infrared Spectra', in *Computer-enhanced Analytical Spectroscopy*, ed. P.C. Jurs, Plenum Press, New York, 1–30, Vol. 3, 1992.

143. M.T. Fahey, L. Irwig, P. Macaskill, 'Meta-analysis of Pap Test Accuracy', *Am. J. Epidemiol.*, **141**(7), 680–689 (1995).

144. M.F. Mitchell, 'Accuracy of Colposcopy', *Consult. Obstet. Gynecol.*, **6**(1), 70–73 (1994).

145. G. Panou-Diamandi, N.K. Uzunoglu, G. Zacharakis, G. Filippidis, T. Papazoglou, D. Koutsouris, 'A One Layer Tissue Fluorescence Model Based on Electromagnetic Theory', *J. Electromag. Waves Appl.*, **12**(8), 1101–1121 (1998).

146. A.J. Durkin, R. Richards-Kortum, 'Comparison of Methods to Determine Chromophore Concentrations from Fluorescence Spectra of Turbid Samples', *Lasers Surg. Med.*, **19**, 75–89 (1996).

147. R. Richards-Kortum, R.P. Rava, M. Fitzmaurice, L.L. Tong, N.B. Ratliff, J.R. Kramer, M.S. Feld, 'A One-layer Model of Laser-induced Fluorescence for Diagnosis of Disease in Human Tissue: Applications to Atherosclerosis', *IEEE Trans. Biomed. Eng.*, **36**(12), 1222–1232 (1989).

148. M.J.C. Van Gemert, W.M. Star, 'Relations Between the Kubelka–Munk and the Transport Equation Models for Anisotropic Scattering', *Lasers Life Sci.*, **1**, 287–298 (1987).

149. H. Zeng, C. MacAulay, D.I. McLean, B. Palcic, 'Reconstruction of In Vivo Skin Autofluorescence Spectrum from Microscopic Properties by Monte Carlo Simulations', *J. Photochem. Photobiol. B: Biol.*, **38**(2/3), 234–240 (1997).

150. J. Qu, C. MacAulay, S. Lam, 'Laser Induced Fluorescence Spectroscopy at Endoscopy: Tissue Optics, Monte Carlo Modeling, and In Vivo Measurements', *Opt. Eng.*, **34**, 3334–3343 (1995).

151. S. Avrillier, E. Tinet, D. Ettori, J.M. Tualle, B. Gelebart, 'Influence of the Emission-reception Geometry on Laser Induced Fluorescence Spectra from Turbid Media', *Appl. Opt.*, **37**(13), 2781–2787 (1998).

152. B.W. Pogue, T. Hasan, 'Fluoropore Quantitation in Tissue Simulating Media with Confocal Detection', *IEEE J. Select. Topics Quant. Electron.*, **12**(4), 959–964 (1996).

153. B.W. Pogue, G. Burke, 'Fiber-optic Bundle Design for Quantitative Fluorescence Measurements from Tissue', *Appl. Opt.*, **37**(31), 7429–7436 (1998).

154. J.K. Dhingra, X. Zhang, K. McMillan, S. Kabani, R. Manoharan, I. Itzkan, M.S. Feld, S.M. Shapshay, 'Diagnosis of Head and Neck Precancerous Lesions in an Animal Model Using Fluorescence Spectroscopy', *Laryngoscopy*, **108**(4), 471–475 (1998).

155. E.W.J. Van der Breggen, A.I. Rem, M.M. Christian, C.J. Yang, K.H. Calhoun, H.J.C.M. Sterenborg, M. Motamedi, 'Spectroscopic Detection of Oral and Skin Tissue Transformation in a Model for Squamous Cell Carcinoma: Autofluorescence versus Aminolevulinic Acid-induced Fluorescence', *IEEE J. Select Topics*, **QE2**, 997–1007 (1997).

156. A.M. Kluftinger, N.L. Davis, N.F. Quenville, S. Lam, J. Hung, B. Palcic, 'Detection of Squamous Cell Cancer and Pre-cancerous Lesions by Imaging Tissue

Autofluorescence in the Hamster Cheek Pouch Model', *Surg. Oncol.*, **1**, 183–188 (1992).

157. I. Pathak, N. Davis, Y.N. Hsiang, N.F. Quenville, B. Palcic, 'Detection of Squamous Neoplasia by Fluorescence Imaging Comparing Porfimer Sodium Fluorescence to Tissue Autofluorescence in the Hamster Cheek Pouch Model', *Am. J. Surg.*, **170**(5), 423–426 (1995).

158. J.M. Nauta, O.C. Speelman, H.L. van Leengoed, P.G. Nikkels, J.L. Roodenburg, W.M. Star, M.J. Witjes, A. Vermey, 'In Vivo Photo-detection of Chemically Induced Pre-malignant Lesions and Squamous Cell Carcinoma of the Rat Palatal Mucosa', *J. Photochem. Photobiol., B: Biol.*, **39**(2), 156–166 (1997).

159. H.J.C.M. Sterenborg, S. Thomsen, S.L. Jacques, M. Motamedi, 'In Vivo Autofluorescence of an Unpigmented Melanoma in Mice. Correlation of Spectroscopic Properties to Microscopic Structure', *Melanoma Res.*, **5**, 211–216 (1995).